Softening-based interface model and nonlinear load-settlement response analysis of piles in saturated and unsaturated multi-layered soils

Citation for published version:
Pham, TA, Nadimi, S & Sutman, M 2024, 'Softening-based interface model and nonlinear load-settlement response analysis of piles in saturated and unsaturated multi-layered soils', *Computers and Geotechnics*, vol. 171, 106331. https://doi.org/10.1016/j.compgeo.2024.106331

Digital Object Identifier (DOI):
10.1016/j.compgeo.2024.106331

Document Version:
Peer reviewed version

Published In:
Computers and Geotechnics

Softening-based interface model and nonlinear load-settlement response analysis of piles in saturated and unsaturated multi-layered soils

Tuan A. Pham

KTH Royal Institute of Technology, Stockholm, Sweden

Heriot-Watt University, School of Energy, Geoscience, Infrastructure and Society, EH14 4AS, Edinburgh, UK

Corresponding email: ta.pham@hw.ac.uk

Sadegh Nadimi

School of Engineering, Newcastle University, Newcastle upon Tyne, NE1 7RU, UK

Email: Sadegh.Nadimi-Shahraki@newcastle.ac.uk

Melis Sutman

Heriot-Watt University, School of Energy, Geoscience, Infrastructure and Society, EH14 4AS, Edinburgh, UK

Email: m.sutman@hw.ac.uk

Abstract

This work presents a simplified method for the nonlinear analysis of the load-displacement response of piles in multi-layered soils. A new interface model based on the disturbed state concept (DSC) is put forth to simulate the interface shear stress-displacement relationship by considering the nonlinear hardening-softening behaviour. In the new model, input parameters can be conveniently calibrated using conventional interface shear tests or on-site tests. The good agreement between predictions and experimental data from interface direct shear tests validated the performance of the proposed DSC model. The DSC model performed better in terms of predictions when compared to the hyperbolic one. Next, the soil-structure interface model and bearing capacity theory are coupled to provide a theoretical framework for the analysis of pile load-transfer in saturated and unsaturated multi-layered soils, where the DSC model is employed to represent base resistance as well as skin friction. This work also discusses the profile of steady-state in-situ matric suction, soil-water characteristic curve, and pore-water pressure of unsaturated soils. The proposed method has the advantage of being used in practice as it is simple to obtain input parameters from laboratory tests, as well as Standard Penetration or Cone Penetration Tests. The proposed framework is finally applied to the analysis of four well-documented case studies. The proposed approach and the static load test results from the field measurements are found to be in satisfactory agreement, indicating that the proposed method performs well. The proposed method is suggested to be utilised for preliminary analysis, planning a suitable programme of loading tests, as well as optimizing the pile design by back analysis of the load test results.

Keywords: Piles; settlement; soil-structure interaction; bearing capacity; softening model; analytical method; disturbed state.

1. Introduction

Pile foundations provide high bearing capacity and have been widely employed to support a variety of applications such as building, deep excavations, slopes, tunnels, and embankments. The load-transfer mechanism of a single pile element includes skin friction resistance along the soil-pile interface and ground reaction at the pile base. There have been several attempts to develop techniques for determining the load-settlement behaviour of individual piles and pile groups, ranging from simplified analytical methods to sophisticated numerical modelling and full-scale in-situ experiments. As the behaviour of piles subjected to vertical force is a complex problem, the experimental approach is regarded as one of the most effective methods for analysing the behaviour of piles. The in-situ tests, however, are difficult, expensive, and time-consuming. In the majority of cases, design engineers prefer to use analytical approaches, particularly in the preliminary design phase.

The load transfer mechanism of piles frequently exhibits a highly nonlinear behaviour due to the intricate interactions between piles and the surrounding soils. The nonlinearity in the load-settlement response of the piles requires simultaneous consideration of both shaft and base resistance (Castelli and Maugeri 2002; Paik and Salgado 2003; Park et al. 2012; Seo et al. 2009; Nadan and Patra 2014). The existing methods have typically used the theoretical load-settlement relationship with the hyperbolic model to investigate the nonlinear behaviour of individual piles (Hirayama 1990; Flemming 1992; Dithinde et al. 2011; Dias and Bezuijen 2018). The hyperbolic model, however, might only be appropriate in the unique scenario of strain hardening that is, the skin friction increases with the relative pile–soil displacement. In reality, skin resistance deterioration has been reported in full-scale field test results where skin friction softening was observed (Reese and O'Neill 1988; Caputo et al. 1991; Briaud et al. 2000; Zhu and Chang 2002; Fioravante 2002; Lee et al. 2003; Fellenius et al. 2004; Zhang et al. 2010; Lehane et al. 2012; Park and Lee 2015; Bohn et al. 2017). The typical characteristic of skin friction softening is that the skin friction increases with the pile-soil displacement before reaching its peak value and then decreases to a residual value (Figure 1). As a result, the skin friction resistance in this situation cannot be reasonably predicted by the hyperbolic models (Zhang and Zhang 2012). Several models, including the dual exponential, the rational-function, and the three-phase piecewise-hyperbolic models, have been recently developed to characterise the softening behaviour of geomaterials and structures (Seol et al. 2009; Zhang and Zhang 2012; Zhu et al. 2021; Chen et al. 2022). These models were, however, more frequently applied to the behaviour of the anchor-soil interface than to that of the pile. Moreover, they are less ideal for application in pile load-transfer analysis as they are defined piecewise and contain many assumed parameters. In the current theoretical load transfer modelling frameworks for piles, the interface stress-displacement model and its parameters were typically chosen based on the epistemic experience of specific researchers and/or back analysis of the in-situ test data, particularly of the pile load-displacement data (Tang and Phoon 2018; Guo et al. 2022; Guo et al. 2023). For this procedure, the tested structural boundary conditions at the pile head were substantially used. This parameter calibration method is indirect, semiempirical, and constrained by the outcomes of the in-situ tests. Therefore, further studies are necessary for modelling the characteristics of pile-soil interfaces, more accurately.

In this study, a simplified method for the nonlinear analysis of the load-settlement response of piles in saturated and unsaturated multi-layered soils which takes into account shaft resistance deterioration and base resistance hardening is presented. Firstly, an adhesion-friction-based model is developed using the disturbed state concept (DSC) to describe the behaviour of the soil-pile interface. The experimental outcomes of interface direct shear tests are then used to verify the proposed DSC model. Next, based on the established integrated interface model, a comprehensive load-transfer modelling framework of piles is developed for analysing the nonlinear load-settlement behaviour. This work also discusses the profile of steady-state in-situ matric suction, soil-water characteristic curve, and pore-water pressure of unsaturated soils that allows to apply the proposed method to piles in unsaturated soils. The effectiveness and accuracy of the proposed approach are evaluated using well-documented field test results gathered from the literature.

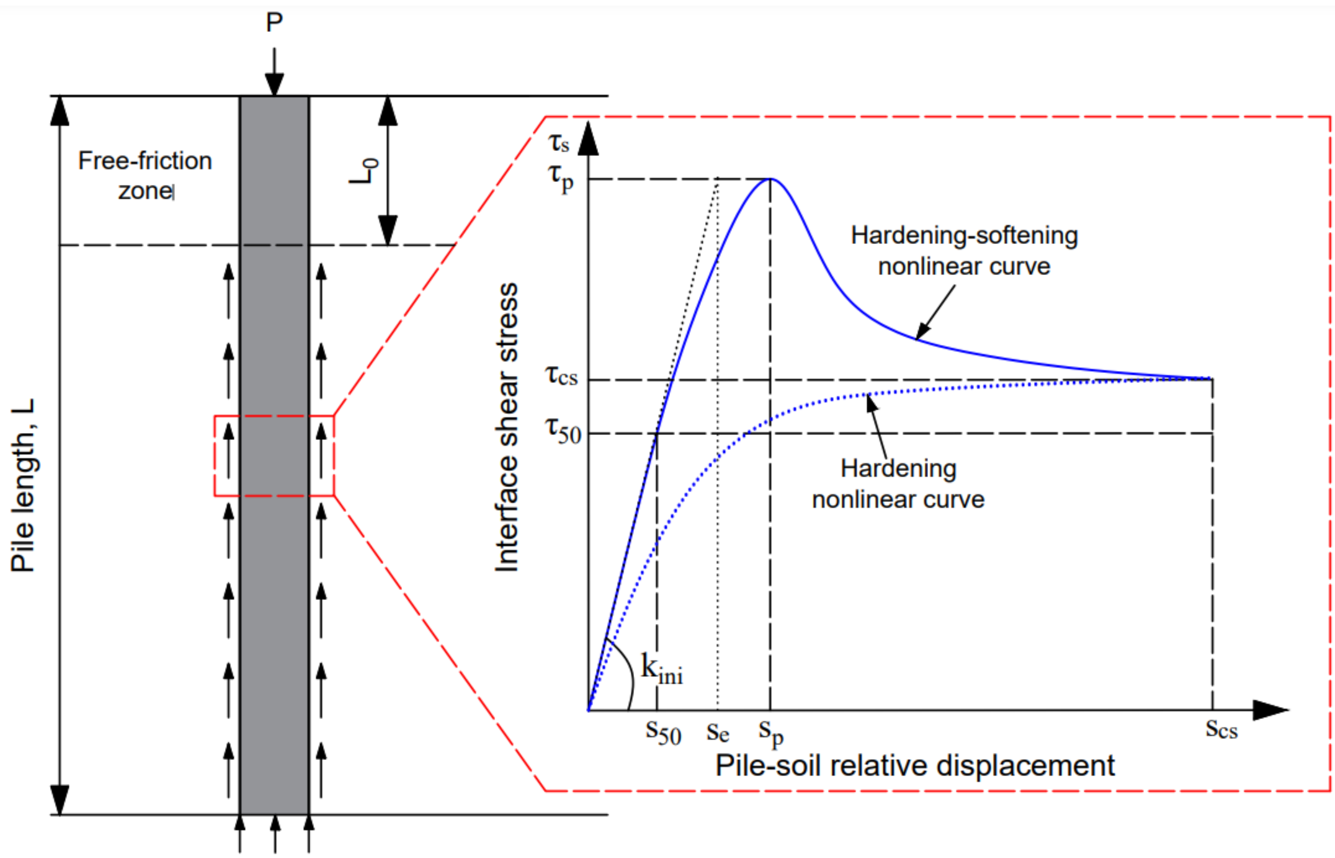

Figure 1. Mobilization of interface shear stress with pile-soil relative displacement

2. Disturbed state-based interface model

In current studies, the nonlinear behaviour involving the interface shear stress and relative displacement is frequently explained by a hyperbolic relationship. The hyperbolic relationship, however, can be applied to special situations, like strain hardening but it is unable to replicate how resistance deteriorates with increasing displacement. In addition, the preceding methods neglected the impact of the soil disturbance on the mobilised shear stress at the soil-structure interface. Finally, these techniques were mainly developed to study the interaction between saturated granular soil and structures and limited research was performed on the unsaturated soil-structure interfaces.

In order to address these shortcomings, a more generalised interface model for load-transfer analysis is still needed. The following simplifications are employed in the development of the present method:

i) Adhesion and interface friction coexist and simultaneously contribute to the resistance of the soil-structure interface.

ii) The soil is thought to remain in a linear elastic state outside of the soil-structure interface.

iii) The nonlinear displacement mostly happens along the disturbed zones surrounding the structure interface.

iv) The structures undergo negligible horizontal deformation.

2.1. Adhesion-friction based interface theory

It is well acknowledged that the geomaterial-structure interface shear strength at a specific displacement is typically made up of interface adhesion $\tau_c(s)$ involving the bonding and interface friction $\tau_\varphi(s)$ involving particle sliding (Chu and Yin 2005; Mitchell and Soga 2005; Pham 2020b; Chen et al. 2022). According to Figure 2, the interface shear strength can be expressed as the sum of the responses as follows:

$$\tau\ (s) = \tau_c(s) + \tau_\varphi(s) \quad (1)$$

where, $\tau\ (s)$, $\tau_c(s)$, $\tau_\varphi(s)$ = total, adhesion, and friction components of the interface shear strength, respectively; s = relative displacement of the interface.

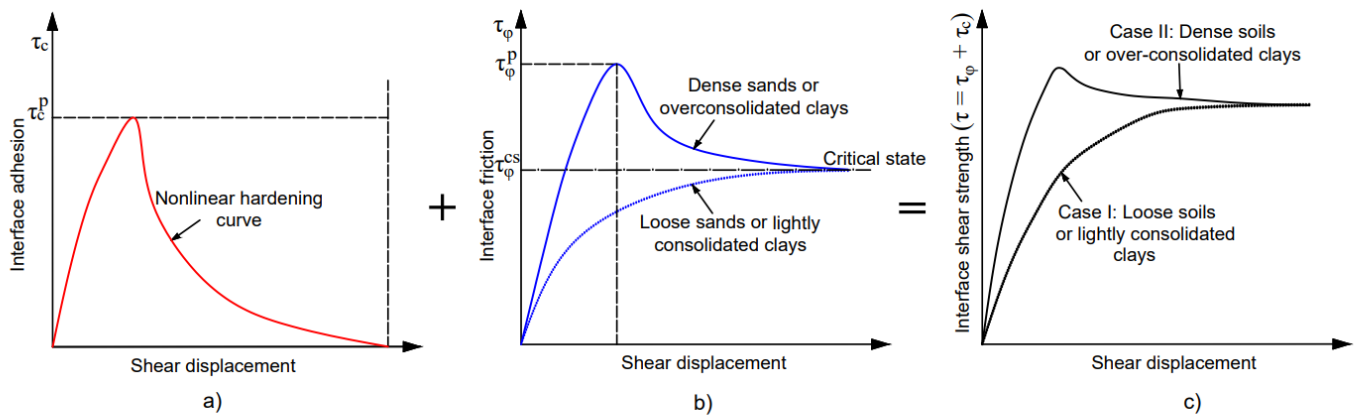

Figure 2. Mobilization mechanism of interface shear resistance: a) adhesion component; b) friction component; c) total interface shear strength

In geotechnical engineering, the term adhesion is used to define the cohesive strength between the structure surface and soils. Interface adhesion first becomes more mobilized with increasing displacement before approaching a constant value as illustrated in Figure 2a. The total adhesion of the soil-structure interface is generally contributed by intermolecular forces like electrostatic and Van der Waals, soil suction from water's surface tension on soil particles, and cementation from the chemical bonding of soil particles (Figure 3a). The general expression for the involvement of several factors in the mobilization of interface adhesion is as follows:

$$\tau_c(s) = \tau_c^i + \tau_c^c + \tau_c^s \quad (2)$$

where τ_c^i = interface adhesion induced by intermolecular force, τ_c^c = interface adhesion induced by cementation, , τ_c^s = interface adhesion induced by suction

Meanwhile, the interface friction is provided by surface-to-surface interaction through a combination of sliding, dilatancy effects, particle crushing, and rearrangement of particles as shown in Figure 3b. However, the relative contributions of each of these factors to the peak shear strength of sands and clays can vary, and not all contributing factors need to appear at the same time for either sands or clays. It is evident that the effects of crushing, dilatancy, and particle rearrangement all have a decreasing influence as value $(\tau_{\varphi}^{p} - \tau_{\varphi}^{cs})$ decreases. This tendency is appropriate for both sands and clays. Clays, for instance, may have the small effects of crushing and dilatancy but the impacts of these factors may increase depending on the over-consolidation ratio or the course-grain amount in clays. It should be also noted that the friction component is influenced by several factors such as surface roughness, relative density, normal pressure, over-consolidation ratio, and structure material type (Potyondy 1961; Uesugi et al. 1990; Martinez and Frost 2017; Wang et al. 2019; Pham 2020c; Ravera et al. 2021; Hashemi et al 2022). Experimental results from direct shear and torsional shear tests suggest that interfaces exhibit strain-hardening behaviour when loose sand soils, normally consolidated or lightly over-consolidated clays are involved, whereas strain-softening behaviour is observed when dense sand or heavily overconsolidated clays are tested (Kishida and Uesugi 1987; Hu and Pu 2004; Toufigh et al. 2017). Interface friction is generally mobilized with increasing interface displacements as shown in Figure 3b. The general description of how various components contribute to the mobilization of interface friction is as follows:

$$\tau_{\varphi}(s) = \tau_{\varphi}^{i} + \tau_{\varphi}^{s} + \tau_{\varphi}^{d} + \tau_{\varphi}^{c} \tag{3}$$

where τ_{φ}^{i} = interface friction induced by interlocking, τ_{φ}^{s} = interface friction induced by sliding, τ_{φ}^{d} = interface friction induced by dilatancy effect, τ_{φ}^{c} = interface friction induced by particle crushing.

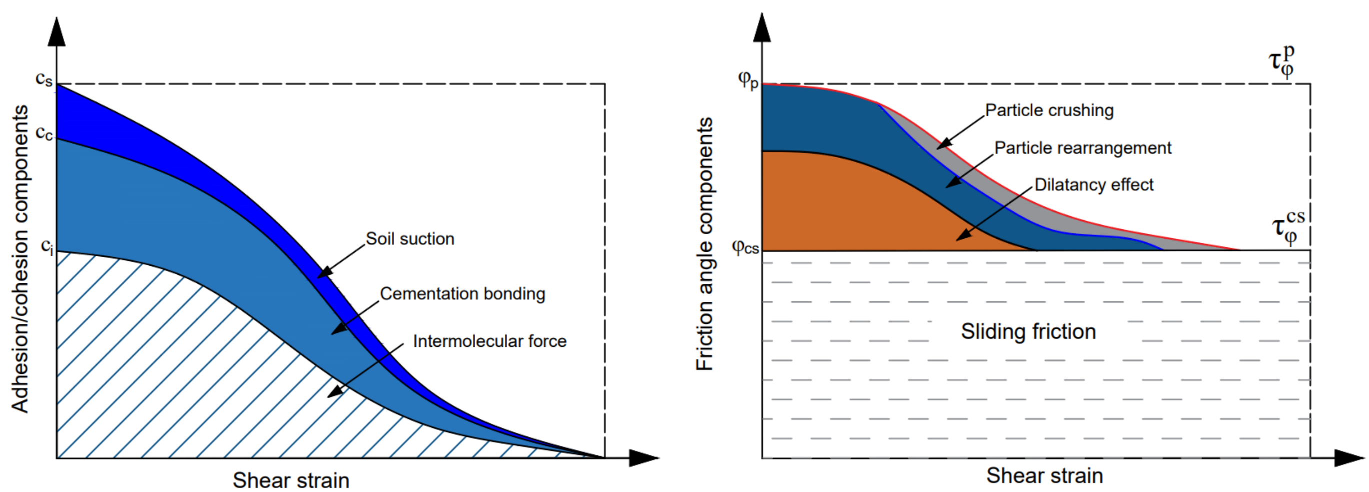

a) b)

Figure 3. Contribution of components on the soil-structure interface resistance: a) Adhesion, b) Friction

The interface adhesion concurrently occurs with interface friction as soil-structure relative displacement increases. However, the ultimate friction and ultimate adhesion are not mobilized at the same displacement. In most cases, the adhesion component is mobilized first, even at relatively small displacements. Following that, the friction component starts to be mobilized as the adhesion reaches the ultimate value. The transition between the adhesion and friction components is represented by the disturbance degree of the interface. If the friction mobilization decrement is greater than the adhesion increment, the interface shear stress may then decline and approach the critical state value (Figure 2c). An interface model, therefore, must be able to simulate the mutual evolution between adhesion and friction components as well as the degree of interface disturbance in order to accurately capture the shear stress-displacement relationship. Here, the DSC theory, which offers a suitable approach, is chosen to characterise the nonlinear behaviours of the soil-structure interface and is presented in the next sections.

2.2. Disturbance function for interface

Desai (2001) presented the idea of the disturbed state, which proposed that the material interface response can be specifically divided into two distinct mechanical states: the relatively intact (RI) state and the fully adjusted (FA) state. Parts of a deforming material are said to be in the RI state if they are still in their original (continuum) state, whereas parts are said to be in the FA state if they are still in their degraded state (discontinues). The elements in the interface zone at the RI and FA states will be randomly distributed and work jointly. With increasing disturbance, the response of the two states changes dynamically, reflecting the deteriorations and discontinuities of the materials from a micro perspective (Figure 4). The adhesion-friction mobilization theory, which was previously described, and the variation between the two RI and FA states are clearly in a logical relationship. Specifically, as friction components increase, the number of elements covered by the FA state must rise and disturbance becomes larger. As a result, the degree of interface disturbance, which reflects the state of the elements in the interaction zone, has a substantial influence on the interface shear strength.

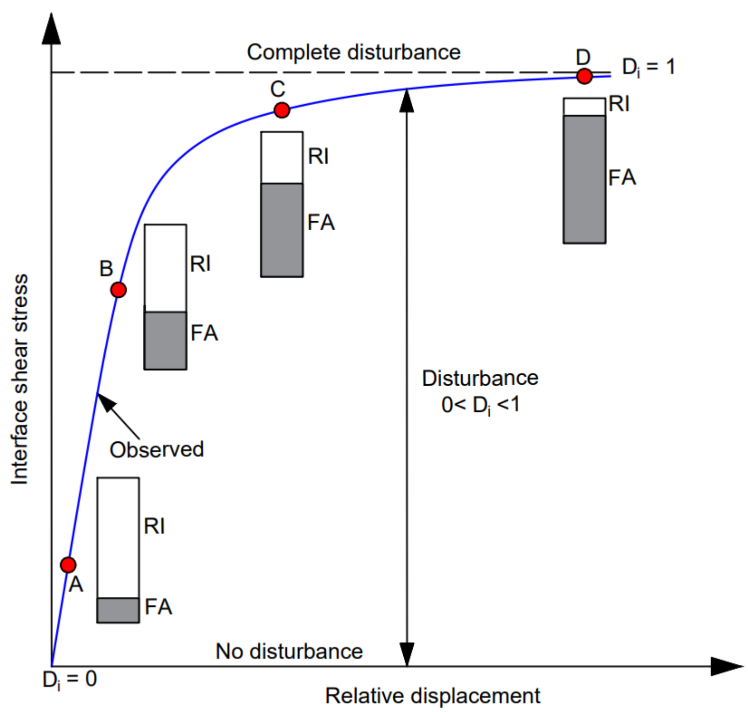

Figure 4. Transition between RI and FA states with disturbance degree

The disturbance degree of an interface is often described by the disturbance function D_i ($0 \leq D_i \leq 1$) which practically indicates the degree of interface damage from an external disturbance. The function D_i will provide a higher value when the interface is subjected to more severe external disturbances. In particular, if $D_i = 0$, the disturbance will completely disappear, and all interface elements will be in the RI state. But, if $D_i = 1$, the interface will be completely disturbed, and all interface elements will be in the FA state. In the modelling framework presented herein, D_i is defined as the proportion of FA state interface elements (n_{FA}) to total interface elements (n_i).

$$D_i = \frac{n_{FA}}{n_i} \tag{4}$$

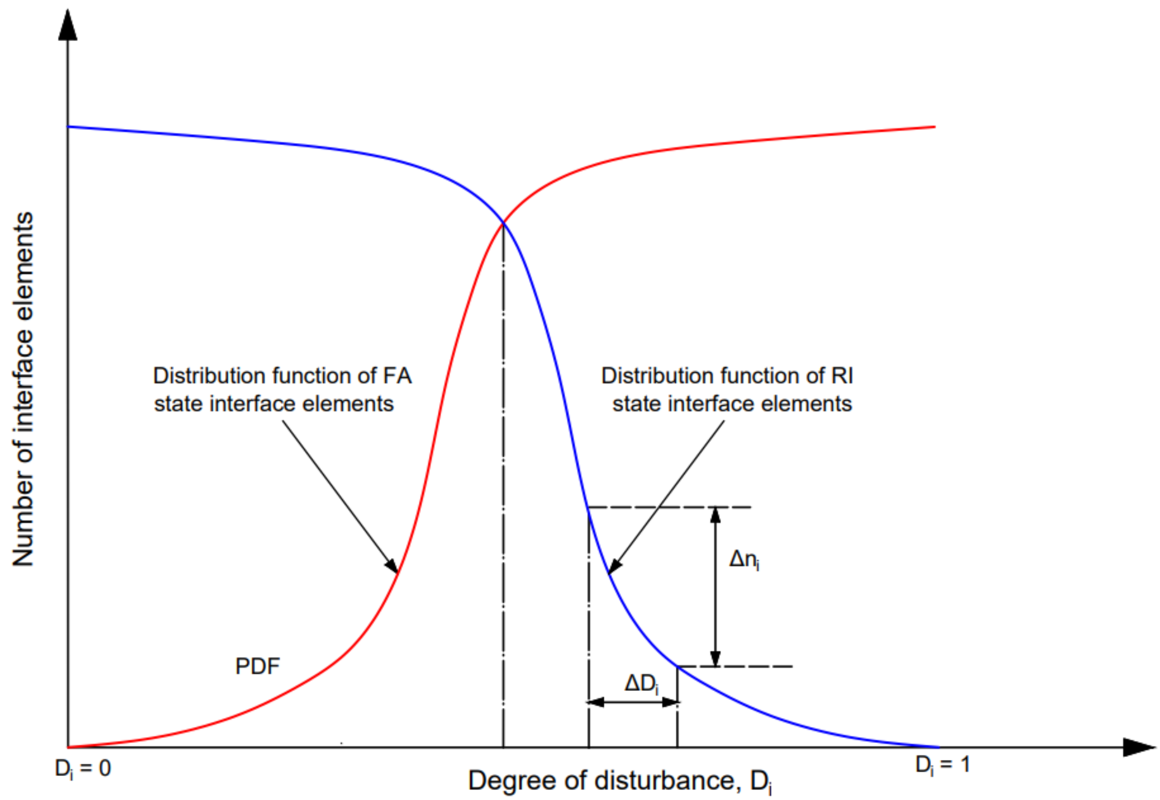

Figure 5. Probability density function and interface elements

The quantity of FA state interface elements and that of RI state interface elements are dynamically changing as soil-structure relative displacement increases, as shown in Figure 5. The Weibull distribution can be used to mathematically describe the shear strength of all interface elements (Desai 2001; Baghini et al. 2018; Huang et al. 2020; Wu et al. 2022). The definition of the probability density function (PDF) is as follows:

$$PDF(x) = \frac{\eta}{\xi}\left(\frac{x}{\xi}\right)^{\eta-1} e^{-(x/\xi)^{\eta}} \tag{5}$$

where η and ξ = two probability parameters, x = the process variable and is defined as the relative displacement between the soil and the structure surface in this work.

The number of interface elements in the FA state increases to n_{FA} when the soil-structure relative displacement reaches value s which can be expressed as follows:

$$n_{FA} = \int_0^s n_i . PDF(x)dx \tag{6}$$

Substituting (5) into (6) gives:

$$n_{FA} = \int_0^s n_i.\frac{\eta}{\xi}\left(\frac{x}{\xi}\right)^{\eta-1} e^{-(x/\xi)^{\eta}} dx = n_i.\left(1 - e^{-(s/\xi)^{\eta}}\right) \tag{7}$$

Replacing Eq. (7) in (4) leads to the following expression:

$$D_i = \left(1 - e^{-(s/\xi)^{\eta}}\right) \tag{8}$$

The disturbance function is rewritten in the simplified form as follows:

$$D_i = 1 - e^{-as} \tag{9}$$

2.3. Interface shear stress-displacement model

The disturbance can also be considered as the deviation of the current deforming state with respect to the initial and final states of the material, which can be defined by using the interface shear stress. The disturbance function for the hardening-softening response of the interface generally can be defined as follows:

$$D_i^h = \frac{\tau}{\tau_p} \tag{10}$$

$$D_i^s = \frac{\tau_p - \tau}{\tau_p - \tau_{cs}} \tag{11}$$

where D_i^h = disturbance function for the hardening phase; D_i^s = disturbance function for the softening phase which is similar to residual factor; τ, τ_p, τ_{cs} = current, peak, and residual shear stress, respectively. It should be noted that the critical state shear stress is defined as a constant stress value even when the interface displacement is continuously increased. When there is no softening phase (only hardening behaviour), the peak and critical state shear stress are identical and are frequently referred to as the ultimate value.

It is necessary to integrate functions D_i^h and D_i^s into a unique disturbance function to achieve a smooth transition between the hardening and softening phases on the shear stress-displacement curve. Eq. (11) is substituted into Eq. (10) to produce:

$$\tau = \frac{D_i^h.D_i^s.\tau_{cs}}{D_i^h + D_i^s - 1} = b.D_i - \Delta\tau \tag{12}$$

where b = model parameter, $\Delta\tau$ = shear stress variation in the softening region. No shear stress reduction occurs after the post-peak zone in the case of hardening behaviour, so $\Delta\tau = 0$ and $b = \tau_p$. However, if the softening behaviour occurs, $\Delta\tau \neq 0$. The method based on the shape of the curve is used to account for the softening behaviour component. The softening curve part is therefore thought to be the result of any hypothetical hardening curve minus the post-peak shear stress decrease zone (coloured area), as illustrated in Figure 6. In this work, the softening portion of the shear stress-displacement curve is assumed to have a hyperbolic shape. The transition curve portion is represented as follows:

$$\Delta\tau = c\left(s^2 - s_p^2\right) \tag{13}$$

where, c = calibration parameter to represent the real form of the curve, S_p = ultimate displacement corresponding to the peak shear stress.

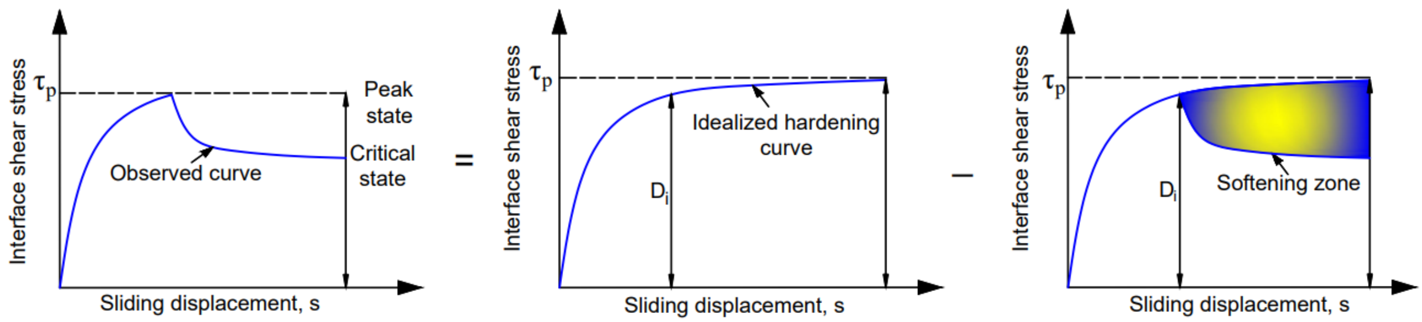

Figure 6. Calculation framework of the hardening-softening curve

Substituting Eqs. (9) and (13) into (12) give interface shear strength:

$$\tau = b\,(1 - e^{-as}) - c\left(s^2 - s_p^2\right) \tag{14}$$

It should be observed that the interface shear stress, however, has a constant value and equals the critical state shear stress when it approaches the critical state condition. This was confirmed by the measurements in reported direct shear tests (Kishida and Uesugi 1987; Mortara et al. 2007; Farhadi and Lashkari 2017; Maghsoodi et al. 2020). Hence, the full form of the proposed equation can be written as follows:

$$\begin{cases} \tau = b\,(1 - e^{-as}) - c\left(s^2 - s_p^2\right) & if\ s \leq s_{cs} \\ \tau = \tau_{cs} & if\ s > s_{cs} \end{cases} \tag{15}$$

where s_{cs} = critical state displacement. It is noted that the proposed model comprises three parameters with clear physical meanings, in which a controls the slope of the hardening curve part, b controls the peak part of the curve, and c controls the softening curve portions. However, all three of these parameters must be coupled in a specific way for the convenience of applicability.

It should be noted that in some special cases, interface shear strength may only consist of interface friction due to the absence of interface adhesion. This is true for structures embedded in coarse soils such as sand and gravel. In almost all other cases, frictional resistance and adhesion, which are mobilized concurrently, combine to produce an interface peak shear strength. However, it is difficult to infer from the results of soil tests how much of the shear strength is provided by friction and adhesion. By using the proposed model, the friction and adhesion components can be determined as follows:

$$\tau_c(s) = c_p.\frac{1-e^{-as}}{1+e^{-as}} \tag{16a}$$

$$\tau_\varphi(s) = \tau\,(s) - \tau_c(s) = b.(1 - e^{-as}) - c_p.\frac{1-e^{-as}}{1+e^{-as}} - c\left(s^2 - s_p^2\right) \tag{16b}$$

where c_p = peak adhesion of the interface.

2.4. Determination of model parameters

When calculating the values of the three model parameters (a, b, c), it is acceptable to use information from characteristic points (also known as interface characteristic parameters) in the shear stress-displacement curve. The initial point, ultimate elastic point, peak stress point, and residual stress points are some important locations of the curve that can be considered. These points yield the peak shear stress τ_p, the displacement corresponding to the peak shear stress s_p, the critical state shear stress τ_{cs}, and the initial shear stiffness k_{ini}. Figure 7 illustrates the boundary conditions to determine these model parameters.

The derivative of the interface shear stress-displacement relationship is written as follows:

$$\frac{d\tau}{ds} = \frac{\partial[b.(1-e^{-as})]}{\partial s} + \frac{\partial[(s_p^2-s^2).c]}{\partial s} = a.b.e^{-as} + 2c.s \quad (17)$$

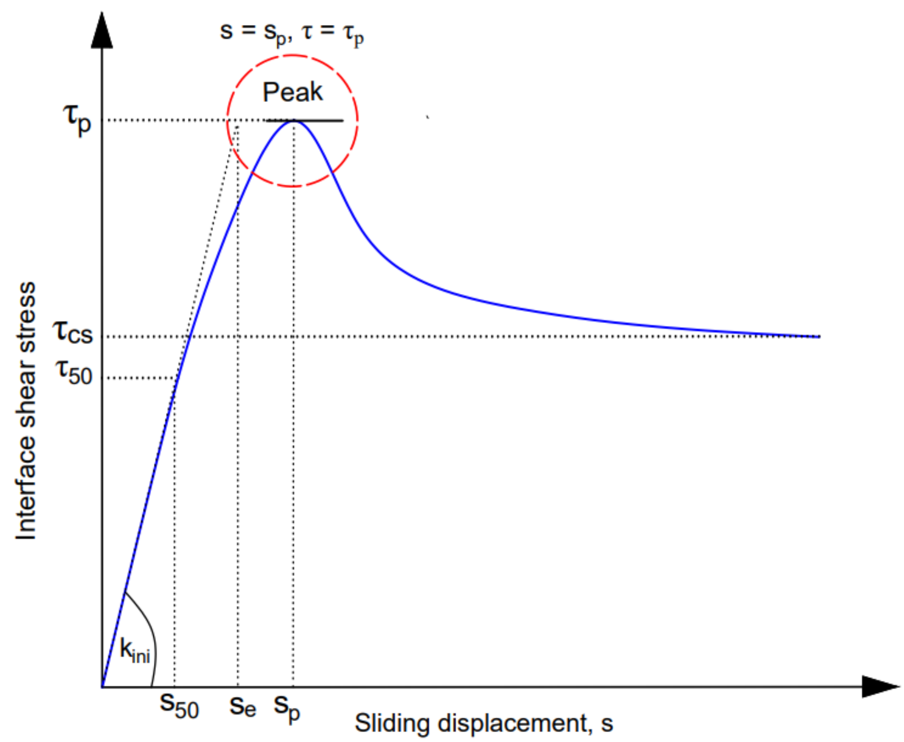

Figure 7. Determination of model parameters based on the boundary conditions.

Boundary condition 1: At displacement s_p, corresponding to the peak shear stress, the disturbance function equals the ultimate disturbance parameter D_i^p.

$$D_i^p = 1 - e^{-as_p} \quad (18)$$

Experimental results show that D_i^p varies in a range of 0.90 and 1. The parameter a is then determined:

$$a = -\frac{\ln(1-D_i^p)}{s_p} \quad (19)$$

Boundary condition 2: At sliding displacement, $\boldsymbol{s} = s_p$, the shear stress equals to peak interface shear stress τ_p

$$\tau_{s=s_p} = b\,(1 - e^{-a.s_p}) = \tau_p \quad (20)$$

The parameter b can then be implied as follows:

$$b = \frac{\tau_p}{1-e^{-a.s_p}} \quad (21)$$

Boundary condition 3: At the origin of the stress-displacement curve, the derivative of interface shear stress over sliding displacement equals to initial shear stiffness:

$$\left.\frac{d\tau}{ds}\right|_{(s=0)} = a.b = k_{ini} \tag{22}$$

If k_{ini} is known, the parameter b could be also determined by:

$$b = -k_{ini}.\frac{s_p}{\ln\left(1-D_i^p\right)} \tag{23}$$

Boundary condition 4: At sliding displacement $\boldsymbol{s} = s_p$, the derivative of interface shear stress over displacement is zero:

$$\left.\frac{d\tau}{ds}\right|_{(s=s_p)} = a.b.e^{-a.s_p} - 2c.s_p = 0 \tag{24}$$

$$c = \frac{a.b.e^{-a.s_p}}{2s_p} \tag{25}$$

2.5. Verification of the interface model

Table 1. Summary of experimental data characteristic parameters

Behaviour type	Test data sets	Soil state	Test case	D_p ($-$)	s_p (mm)	τ_p (kPa)	τ_{cs} (kPa)	a (mm^{-1})	b (kPa)	c (kPa/mm)
Hardening behaviour	Zhang and Zhang (2006)	Loose dry gravel	**R = 0.1 mm**	0.999	20	138.1	138.1	0.35	138.2	0.001
			R = 1.0 mm	0.999	20	151.8	151.8	0.35	152.0	0.001
			R = 10 mm	0.999	20	212.3	212.3	0.35	212.5	0.002
	Evgin and Fakharian (1997)	Loose dry sand	**σ = 100 kPa**	0.996	2.93	208.3	208.3	1.88	209.1	0.269
			σ = 300 kPa	0.996	2.93	267.8	267.8	1.88	268.9	0.346
			σ = 500 kPa	0.996	2.93	350.9	350.9	1.88	352.3	0.453
	Liu et al. (2014)	Unsaturated silty clay	**σ = 200 kPa**	0.999	8.76	273.5	273.5	0.79	273.8	0.012
			σ = 300 kPa	0.999	8.76	345.2	345.2	0.79	345.5	0.016
			σ = 400 kPa	0.999	8.76	468.6	468.6	0.79	469.1	0.021
Hardening-softening behaviour	Hu and Pu (2004)	Dense dry sand	**σ = 100 kPa**	0.992	0.96	120.9	70.15	5.03	121.9	2.554
			σ= 200 kPa	0.992	0.96	187.3	1338	5.03	188.8	3.957
			σ = 400 kPa	0.992	0.96	368.6	2633	5.03	371.6	7.787
	Maghsoodi et al. (2020)	Over consolidated saturated clay	T = 5^0C	0.94	1.26	82.5	66.90	2.23	87.8	4.666
			T = 22^0C	0.94	1.26	84.7	72.52	2.23	90.1	4.790
			T = 60^0C	0.94	1.26	93.2	68.38	2.23	99.1	5.271
	Di Donna et al. (2016)	Saturated clay	**σ = 50 kPa, T = 20^0**	0.95	0.54	32.9	28.7	5.55	34.6	8.895
			σ = 50 kPa, T = 60^0	0.95	0.54	40.0	36.12	5.55	42.1	10.814
			σ = 100 kPa, T = 20^0	0.95	0.54	56.1	49.48	5.55	59.1	15.167
			σ = 100 kPa, T = 60^0	0.95	0.54	80	67.05	5.55	84.2	21.628
	Wang et al. (2019)	Dense dry sand	C_u = 1.85	0.98	1.20	83.2	44.4	3.26	84.9	2.306
			C_u = 2.81	0.98	1.20	69.6	58.8	3.26	71.0	1.929
			C_u = 5.20	0.98	1.20	58.4	44.4	3.26	59.6	1.619

Note: Bold values are baseline cases that used to determine input parameters. The baseline is selected according to the following rules: room temperature, smallest pressure and roughness, largest coefficient of uniformity.

The shear test results reported in the literature are used to validate the proposed interface model. The performance of the proposed model is assessed separately based on its applicability to model two scenarios: only hardening behaviour and hardening-softening behaviour. Seven data sets therefore are used to evaluate the model performance, in which three datasets are available for loose soils and four data sets are available for dense soils. Characteristic reference values of the experimental data, which were taken from these selected studies, are provided in Table 1. It should be noted that the values of peak and critical state shear stress are the same in the case of loose soils with only a hardening response. However, the values of peak and critical state shear stress differ in dense soils with a hardening-softening response. The proposed model was further strengthened by comparison with the hyperbolic model in this study.

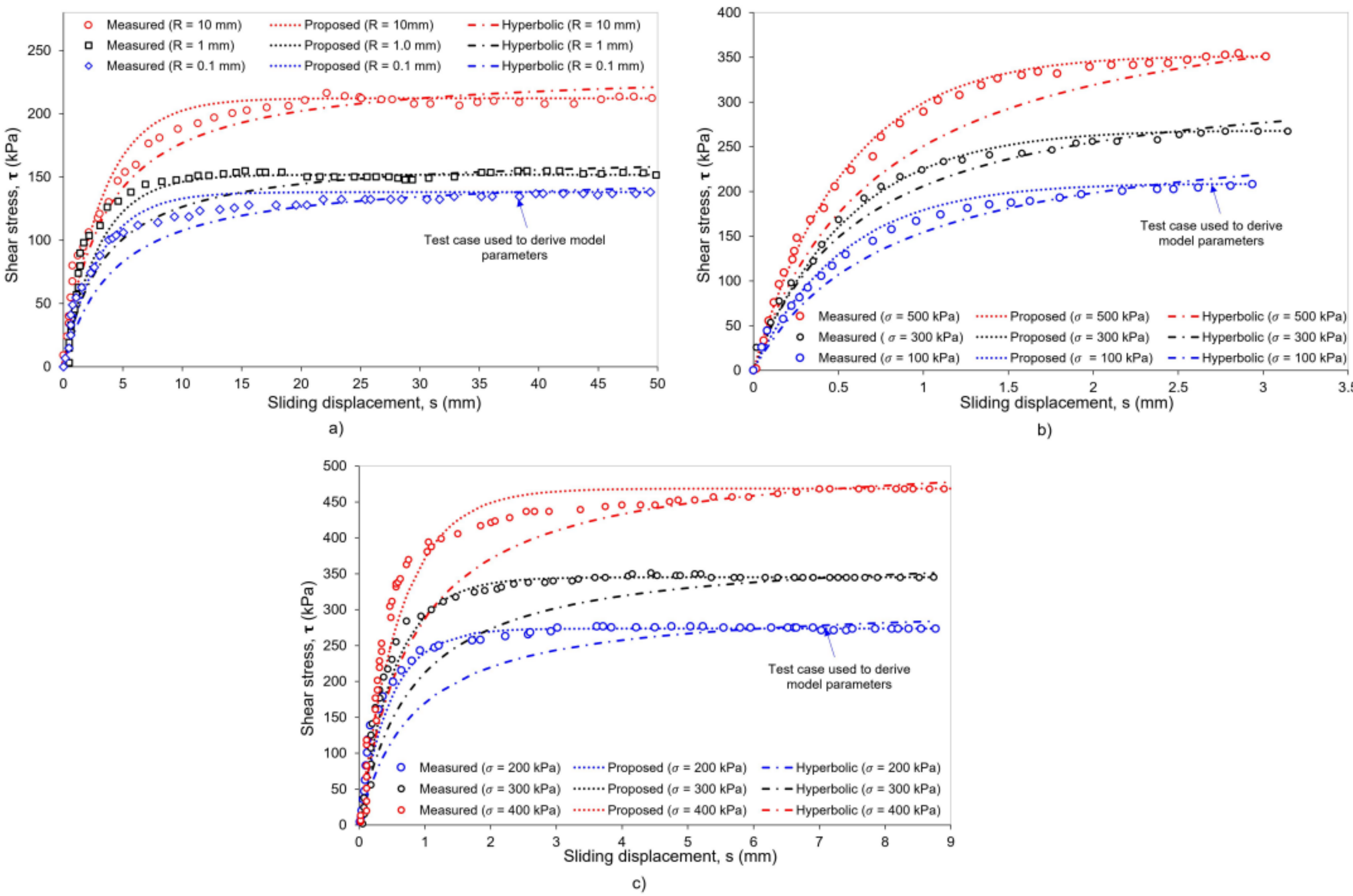

Figure 8. Comparison between the predicted and measured outcomes for loose soils: a) test data after Zhang and Zhang (2006); b) test date after Evgin and Fakharian (1997); c) test data after Liu et al. (2014)

Figure 8 compares the predicted outcomes from the proposed model with the hyperbolic model and measured data for loose soils. It should be noted that each test data set uses the same input parameters for analytical models to predict interface shear stress-displacement curves under different scenarios, except for peak shear stress. The results predicted by the proposed model matched well with the experimental data, indicating that the model utilized in this study is appropriate for describing the interface shear stress mobilized with displacement. It should be noted that the proposed model and test results have a better agreement than the hyperbolic model. Moreover, the hyperbolic model consistently demonstrates that shear stress rises with increasing displacement, even at high displacement values.

Nonetheless, the test results demonstrate that as displacement is increased to a large value, shear stress approaches a constant value, which leads to a better performance as compared to the hyperbolic model.

The predictions of the proposed model are compared with the hyperbolic model and measured data for dense soils or over-consolidated soils in Figure 9. According to the measured data, the shear stress increases with increasing sliding displacement to a peak value, then starts to decrease, and finally reaches a constant critical state value. As can be seen, the proposed model accurately describes three crucial transition phases of the curve (hardening, softening, and critical state zones), indicating that it is a good fit for describing the shear stress-displacement curve, particularly for characterizing the softening behaviour. On the other hand, for the hyperbolic model, which only considers the hardening behaviour, the predicted curves greatly deviate from the experimental values. The hyperbolic model, therefore, fails to reflect the post-peak behaviour of the interface shear stress.

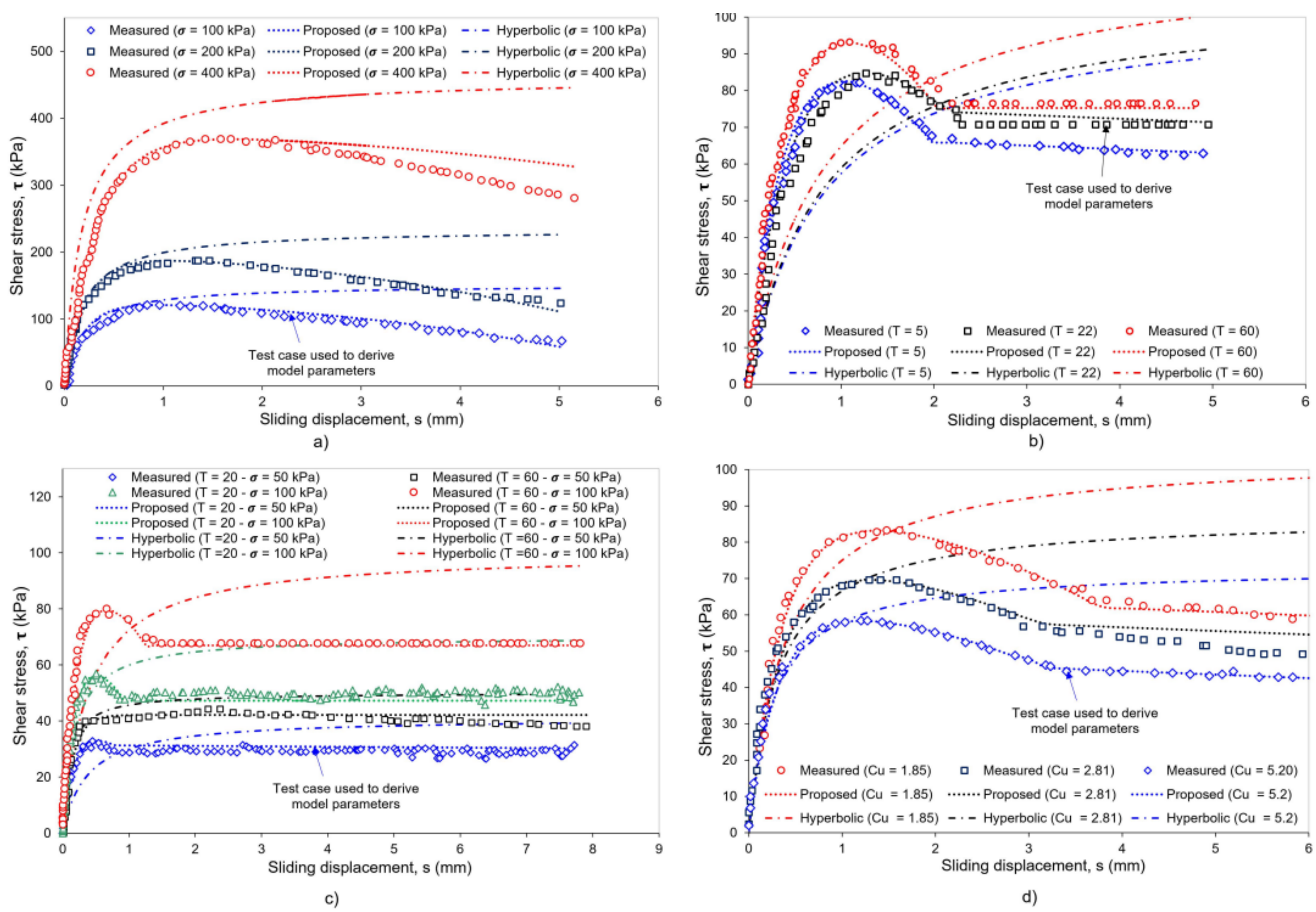

Figure 9. Comparison between the predicted and measured outcomes for dense soils: a) test data after Hu and Pu (2004); b) test data after Maghsoodi et al. (2020); c) test data after Di Donna et al. (2016); d) test data after Wang et al. (2019)

By using the test data from two cases, the proposed model illustrates how adhesion and friction components contribute to the interface shear strength, as shown in Fig. 10a for loose soils and Fig. 10b for dense soils. As can be observed, the adhesion rises quickly with increasing sliding displacement and approaches a peak value (in this case $\tau_c^p = 12\ kPa, s_c = 0.47mm$) which indicates that the displacement range to mobilize ultimate adhesion is comparatively small. The friction component, however, mobilizes significantly and approaches a limiting value in the case of loose soils or later displays softening behaviour in the case of dense soils. It is important to note that the contribution of friction to interface shear stress is significantly higher than that of adhesion.

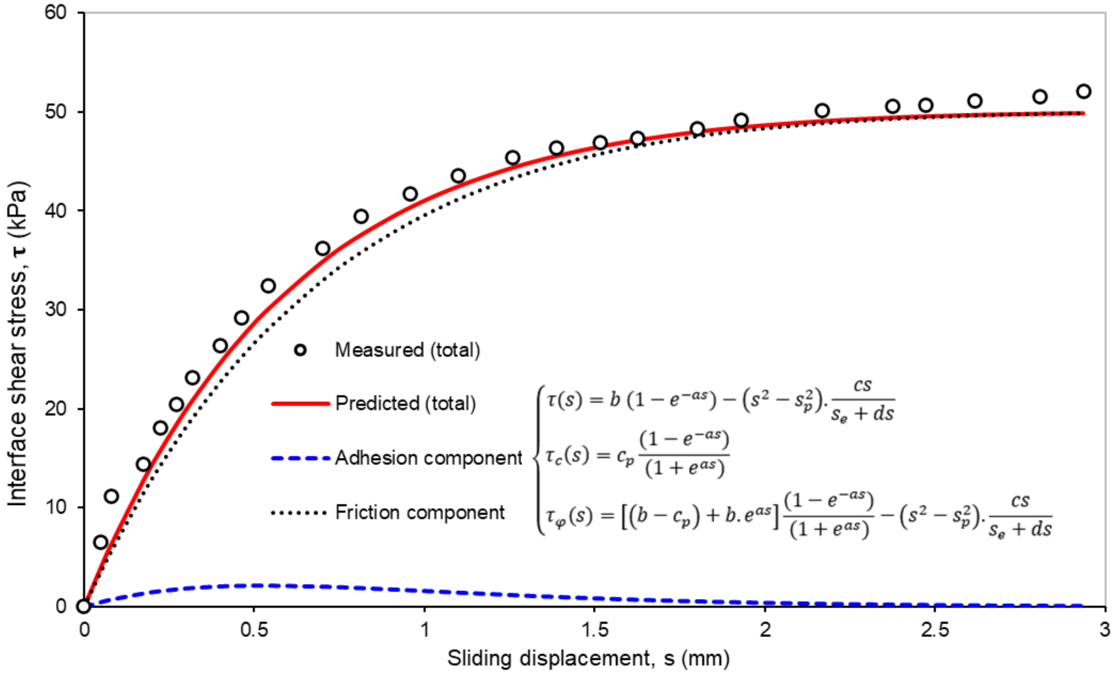

a)

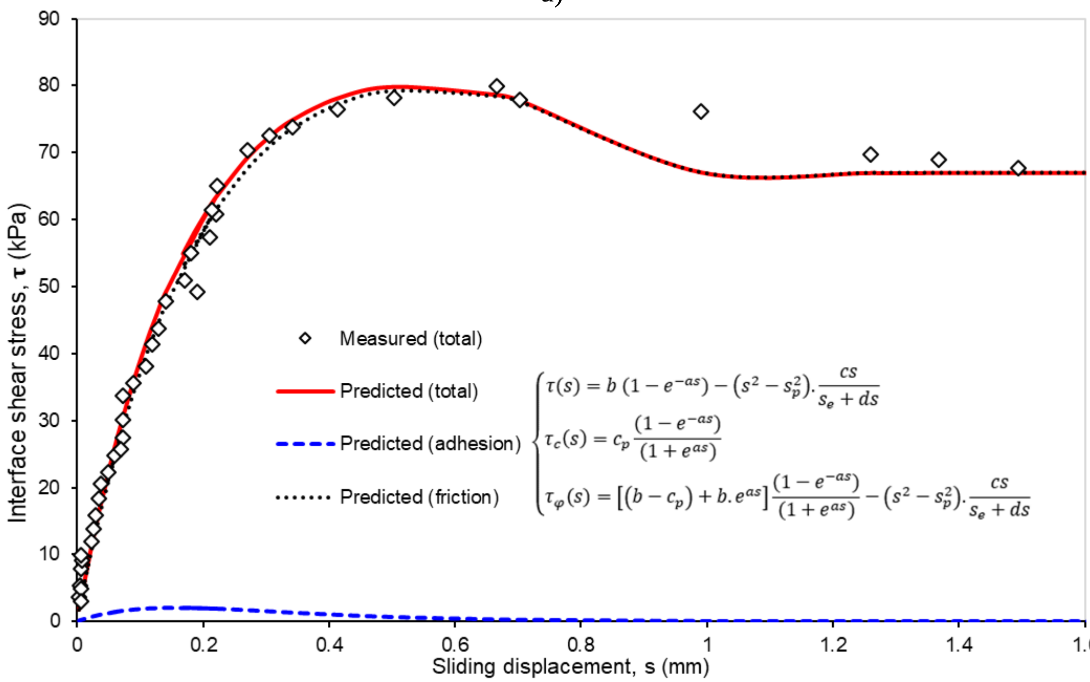

b)

Figure 10. Evolution contribution of adhesion and friction components to interface shear stress: a) Test data from Evgin and Fakharian 1997 ($\sigma = 50$ kPa); b) Test data from Di Donna et al. 2016 ($\sigma = 100$ kPa, T = 60°C)

3. Load-settlement response analysis of piles using DSC model

The DSC model demonstrated success in predicting the interface shear stress-displacement relationship as well as accurately captured the hardening-softening behaviour in the previous section. As a result, the proposed interface model is extended and combined with bearing capacity theory to create a more straightforward method for analysing the load-settlement response of piles in multi-layered soils.

3.1. Load capacity of a single pile

The ultimate load capacity of a single pile, Q_{ult}, is typically considered to consist of two components. The first component, referred to as skin friction or shaft friction, is caused by interaction between the pile shaft and surrounding soils, while the second part, referred to as end-bearing capacity, is caused by ground reaction at the pile base. Depending on the strength and stiffness of the soil layers, a specific vertical displacement may be required to mobilize the ultimate base and shaft resistance. However, in any conditions, the ultimate load capacity of a pile can be written as follows:

$$Q = Q_s + Q_b - W_p = \tau_s . A_s + q_b . A_b - \gamma_p . V_p \tag{26}$$

where W_p = weight of the pile, τ_s = unit skin friction, q_b = unit base resistance, A_s = pile shaft area, A_b = pile cross-sectional area, γ_p = unit weight of the pile, V_p = volume of the pile.

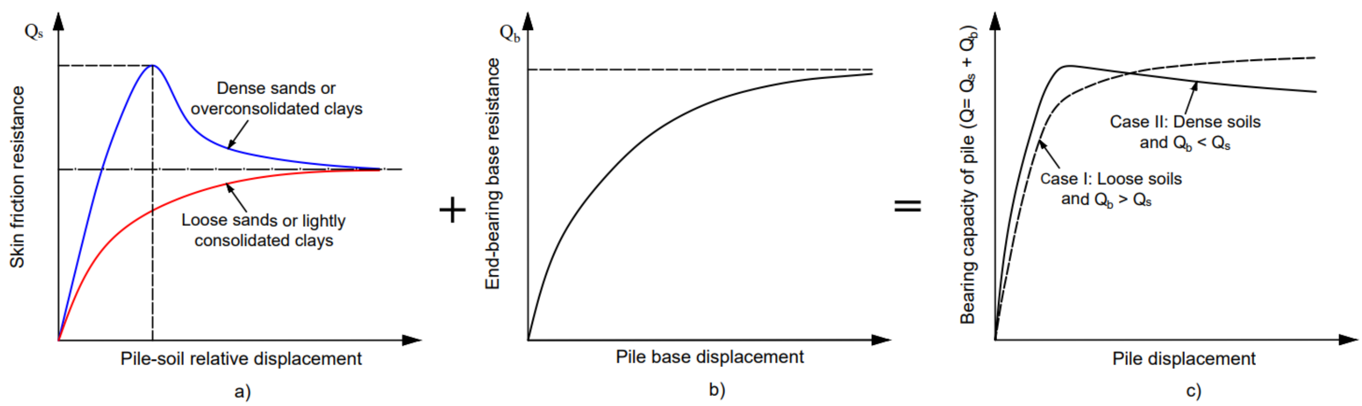

Figure 11. Schematic of mobilized load-settlement curves for a single pile: (a) skin friction versus displacement; (b) base resistance versus displacement; (c) total bearing capacity versus displacement

The skin friction, which is mobilized by the relative displacement of the pile and the soil, may exhibit only hardening or hardening-softening behaviour depending on the stiffness of the surrounding soils. Figure 11a demonstrates the relationship between skin friction and pile displacement. The soil below the base of the pile, on the other hand, is severely constrained from moving in the lateral and vertical directions and is mainly subjected to compressive pressures. Hence, end-bearing resistance at the pile base frequently increases with the increasing settlement. Likely, the soil element at the pile base does not respond to applied loads with a peak stress-strain response or strain softening because of the significant overburden pressure. Instead, until a critical condition is reached, it exhibits only hardening behaviour. Figure 11b depicts a model of the relationship between displacement and base resistance.

In general, the load settlement curve of a single pile is frequently impacted by the soil type and density, thus exhibiting the two following forms: If the soils are dense and the skin friction is greater than the base resistance, the pile will behave in a hardening-softening way. The pile can display hardening behaviour if there are loose soils present or if base resistance is larger than the skin friction resistance (Figure 11c).

3.2. Nonlinear model of skin friction resistance

The skin friction resistance over the embedded length of the pile is calculated by multiplying the unit interface shear strength and surface area of the pile shaft, as indicated in the equation below:

$$Q_s = \tau_s . A_s = \begin{cases} \left[b\,(1-e^{-as}) - c\left(s^2 - s_p^2\right)\right] . A_s & if\ s \le s_{cs} \\ \tau_{cs} . A_s & if\ s > s_{cs} \end{cases} \tag{27}$$

Which, the interface model in the previous section is extended to include the estimation of controlling parameters

$$a = -\frac{\ln\,(1-D_i^p)}{s_p}$$

$$b = \frac{\tau_p}{1-e^{-a.s_p}}$$

$$c = \frac{a.b.e^{-a.s_p}}{2s_p}$$

The model parameters must be known in order to determine the skin friction resistance using Equation (27). The proposed model has three parameters, which can be directly derived based on interface shear experiments or by applying the effective stress principles.

Ultimate and residual skin friction (τ_p and τ_{cs})

The peak and residual points of the interface shear stress-displacement test curve can be used to determine the ultimate skin friction τ_p and critical state skin friction τ_{cs}. In the absence of test results, τ_p and τ_{cs} can be estimated using a formula based on soil properties obtained from laboratory or in-situ studies. The drained condition is predicted using the effective stress approach or so-called β-method (Pham 2022a). The following equations can be used to determine the ultimate unit of skin friction based on Coulomb's friction law:

$$\tau_p = c' + K.(\sigma_z')_i . tan\delta_p = c' + \left(1 - sin\varphi_p\right).(OCR)^{0.5}. tan\left(R_i . \varphi_p\right).(\sigma_z')_i \tag{28a}$$

$$\tau_{cs} = c' + K.(\sigma_z')_i . tan\delta_{cs} = c' + (1 - sin\varphi_{cs}).(OCR)^{0.5}. tan(R_i . \varphi_{cs}).(\sigma_z')_i \tag{28b}$$

$$\varphi_p = \varphi_{cs} + 0.8\psi \tag{29}$$

$$(\sigma_z')_{sat} = \sigma - u_w(1-D) \tag{30a}$$

$$(\sigma_z')_{unsat} = (\sigma - u_a) + \psi.[\theta + S.(1-\theta)] + u_w.D \tag{30b}$$

where, φ_p and φ_{cs} = peak and critical friction angle respectively, δ_p and δ_{cs} = friction angle of the pile-soil interface at peak and residual state, respectively, ψ = dilatancy angle, R_i = interfacial friction coefficient which ranges from 0.8 to 1.0 depending on the material and roughness, OCR = over-consolidated ratio, $\sigma = \gamma z$ = normal stress, γ = unit weight of soils, z = depth from the ground surface, $(\sigma'_z)_i$ = vertical effective stress that is calculated at the centre of soil layer i, $(\sigma'_z)_{sat}$ = vertical effective stress of saturated soils, $(\sigma'_z)_{unsat}$ = vertical effective stress of unsaturated soils; u_a = pore-air pressure, u_w = pore-water pressure, θ = volumetric water content, S = degree of saturation, D = particle contact area ratio, ψ = soil suction.

Pore-water pressure of unsaturated soils

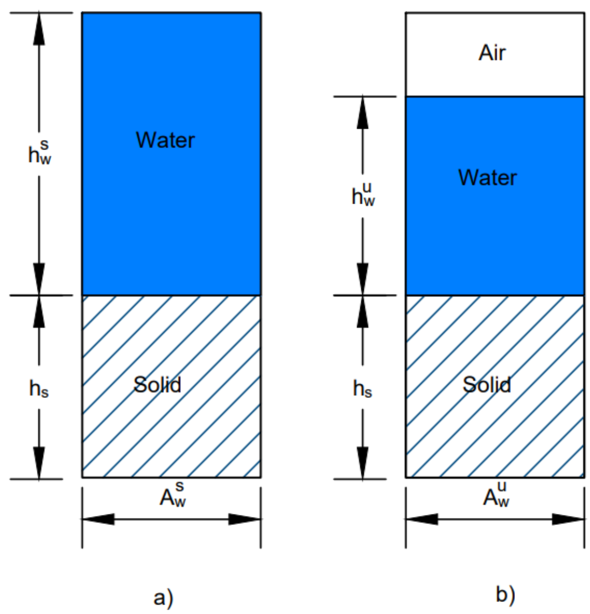

Figure 12. Soil phases in idealized soil model: a) saturated soil and b) unsaturated soil

Considering an idealized soil model with saturated and unsaturated conditions as shown in Figure 12, the pore-water pressure in unsaturated soil (u_w) could be expressed as follows:

$$u_w = \gamma_w.\frac{V_w^u}{A_w^u} = \gamma_w.\frac{V.\theta_w.S}{A_w^u} = \gamma_w.h_w^u.S \qquad (31)$$

where h_w^u = water column height; S = degree of saturation; γ_w = unit weight of water; V_w = total water volume; A_w = cross-section area filled by water.

The pore-water pressure under hydrostatic conditions of unsaturated soils in situ is estimated by replacing the water column height (h_w^u) with the water depth, which is determined as depth calculated from the groundwater table (z_w).

$$u_w = \gamma_w.z_w.S \qquad (32)$$

Estimating soil suction with the Soil-Water Characteristic Curve

The concept of soil suction, which refers to the free energy state of soil water, is frequently used to describe the behaviour of unsaturated soils (Edlefsen and Anderson 1943; Pham and Sutman 2022a; Pham et al. 2023a). Total soil suction is the result of the combined action of matric suction and osmotic suction. The thermodynamic relationship between suction and partial pressure of the pore-water vapour can be expressed as follows:

$$\psi = (u_a - u_w) + \pi = -\frac{RT\rho_w}{\omega_v} ln\left(\frac{u_v}{u_{v0}}\right) = -\frac{RT\rho_w}{\omega_v} ln(RH) \tag{33}$$

where ψ = soil suction or total suction; $(u_a - u_w)$ = matric suction that is associated with the capillary component; π = osmotic suction that is associated with the solute component (salt content of pore water); R = universal gas constant [8.31432 J/(mol.K)]; T = absolute temperature [$T_K = 273 + T_{℃}$]; ω_v =molecular mass of water vapour [18.016 kg/kmol]; ρ_w = water density; u_v =partial pressure of pore-water vapor (kPa); u_{v0} = saturation pressure of water vapour over a flat surface of pure water at the same temperature. The relative vapour pressure in the air immediately adjacent to the water, u_v/u_{v0}, is called relative humidity (RH).

There is an ongoing discussion on the role of osmotic suction, despite the fact that the engineering behaviour of unsaturated soils is described by the inclusion of soil suction as "effective" stress or suction stress, as seen in equation (30b). Tests on compacted soils by Leong and Abuel-Naga (2018) revealed that osmotic suction has a negligible impact on the shear strength of soils. As a result, in the following presentation, the soil suction will be compatible with the term matric suction, which describes the engineering behaviour of unsaturated soils $(\psi = u_a - u_w)$. Equation (30b) therefore should be rewritten in the term of matric suction as follows:

$$\left(\sigma_z^{'}\right)_{unsat} = (\sigma - u_a) + (u_a - u_w).[\theta + S.(1-\theta)] + u_w.D \tag{34}$$

The measurement of the matric suction can be achieved either directly via the use of tensiometers, filter paper (contact method), oedometer tests, null-type pressure plate (axis translation technique), or indirectly through the use of thermal and electrical conductivity sensors (Pham and Sutman 2022b). These techniques quantify how the moisture content varies in relation to the change in matric suction, which is also well-known as the Soil-Water Characteristic Curve (SWCC). It is important to note that, as Figure 13 illustrates, SWCC often exhibits hysteresis concerning the wetting and drying regions of the curve, where two distinct matric suction pressures may exist for the same volumetric water content. A number of researchers (Brooks and Corey 1964, Van Genuchten 1980, and Fredlund and Xing 1994) proposed the fitting equations to plot SWCC based on simple regression of only some of the available test points because it is time-consuming to measure matric suction at all different moisture levels. The equation by Fredlund and Xing (1994) is used in this work to determine SWCC as follows:

$$S = \frac{C(\psi)}{\{ln[2.7183 + (\psi/a)^n]\}^m} \tag{35}$$

$$C(\psi) = 1 - \frac{ln(1+\psi/\psi_r)}{ln(1+10^6/\psi_r)} \tag{36}$$

where a = fitting parameter which is primarily a function of the air-entry value of soil; n = fitting parameter which is primarily a function of water extraction rate from the soil once the air-entry value has been exceeded; m = fitting parameter which is primarily a function of residual water content; $C(\psi)$ = correction factor which is primarily a function of residual suction (ψ_r) corresponding to residual water content.

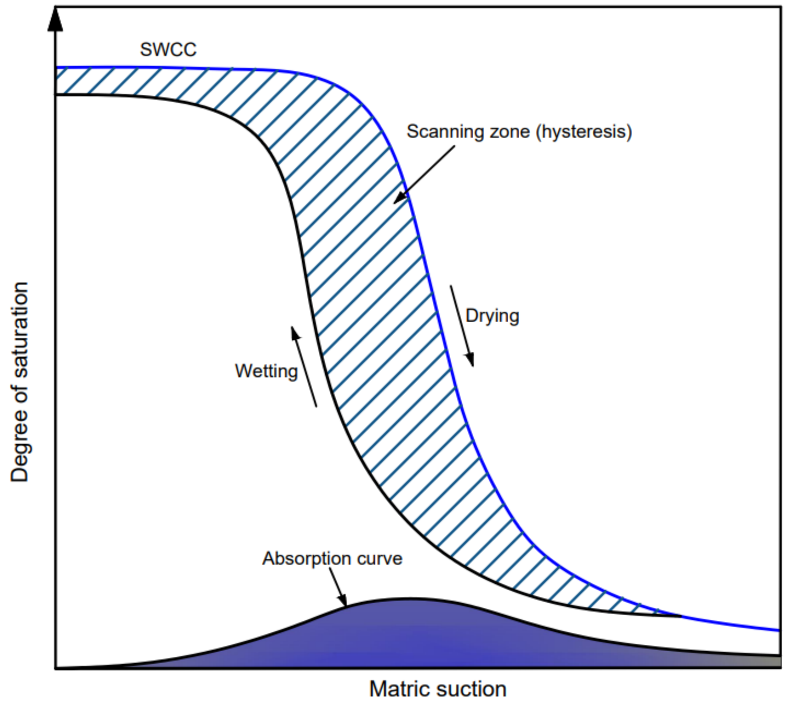

Figure 13. Illustration of SWCC for unsaturated soils

It should be mentioned that soil density, which may be impacted by overburden pressure during pile installation, is one of the factors that significantly affect matric suction and pore-water pressure in situ. It is therefore crucial to take soil density into account while assessing the engineering behaviour of unsaturated soils (Pham 2022b; Pham and Sutman 2023). In order to overcome the uncertainty of SWCC related to the overburden pressure, the density-dependent SWCC model of Pham et al. (2023c) may be considered a promising option due to its simplicity, which is expressed by:

$$\begin{cases} S_{e_i} = S_{e_0} = \dfrac{1}{ln\left(2.7127+[\psi_{e_0}/a]^n\right)^m} \\ \psi_{e_i} = \psi_{e_0} \times \sqrt{\dfrac{e_0}{e_i} . \left(\dfrac{1+e_i}{1+e_0}\right)^{1-\delta}} \end{cases} \quad (37)$$

Where e_i = void ratio corresponds to the current overburden pressure; e_0 = void ratio corresponds to the initial overburden pressure (or confining pressure used in laboratory SWCC tests).

Vertical profile of steady-state matric suction

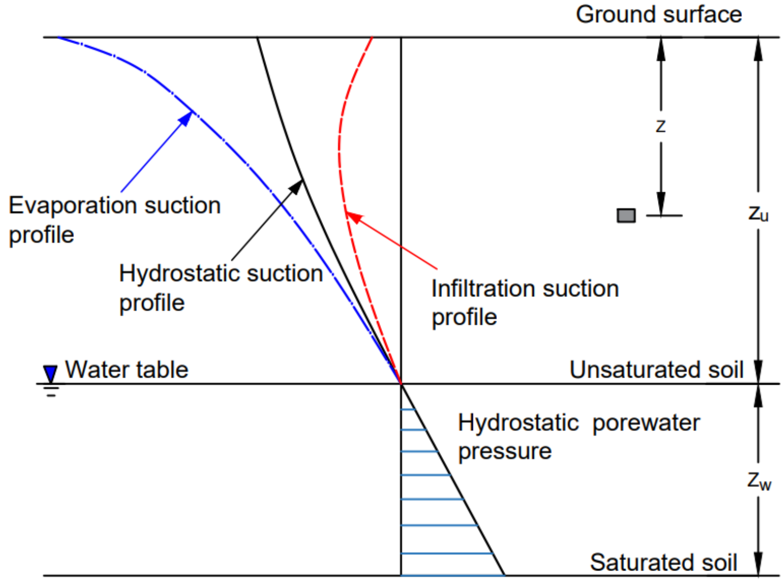

Figure 14. Suction distribution profile with different boundary conditions

In horizontally stratified unsaturated soils, the vertical distribution of matric suction is typically highly dependent on environmental variables such as boundary drainage conditions and infiltration due to precipitation or evaporation rates (Pham et al. 2023d). As a result, the matric suction varies with the depth and permeability conditions, as shown in Figure 14. The theoretical approach presented in this paper can be directly applied to extend the classical limit analysis to unsaturated soil environments. The controlling flow equation can be solved with suitable initial and boundary conditions to create the mathematical prediction of matric suction profiles. The vertical unsaturated soil flow rate for steady-state profiles can be expressed as follows, using Darcy's law:

$$q = -k_u.\left(\frac{d\psi/\psi_0}{dz/z_u} + 1\right) = -k_u.\left(\frac{d\psi}{\beta.dz} + 1\right) \quad (38)$$

where z_u = unsaturated soil thickness or equals the distance from the groundwater table to the ground surface (Fig. 14); ψ_0 = initial matric suction; $\beta = \psi_0/z_u$ = suction distribution rate; k_u = unsaturated hydraulic conductivity dependent on suction. To describe the characteristic of unsaturated hydraulic conductivity, Gardner's model (1958) is used:

$$k_u = k_s e^{-\psi/AEV} \quad (39)$$

Where AEV =air-entry value; k_s = saturated hydraulic conductivity

Substituting Eq. (39) in Eq. (38) leads to:

$$q = -k_s e^{-\psi/AEV}.\left(\frac{d\psi}{\beta.dz} + 1\right) \quad (40)$$

$$-\frac{\beta.q}{k_s}dz = -e^{\left(-\frac{\psi}{AEV}\right)}d\psi + \beta.e^{\left(-\frac{\psi}{AEV}\right)}dz \quad (41)$$

$$dz = \frac{e^{\left(-\frac{\psi}{AEV}\right)}d\psi}{\frac{\beta.q}{k_s}+\beta.e^{\left(-\frac{\psi}{AEV}\right)}} = -\frac{AEV}{\beta}.\frac{d\left\{\frac{q}{k_s}+e^{\left(-\frac{\psi}{AEV}\right)}\right\}}{\frac{q}{k_s}+e^{\left(-\frac{\psi}{AEV}\right)}} \quad (42)$$

A steady-state flow rate q is negative ($q < 0$) for downward infiltration and is positive ($q > 0$) for upward evaporation. An analytical solution for the suction profile could be obtained by integrating the above equation and imposing the boundary conditions of zero suction at the water table ($z = 0$).

$$\int_0^z dz = -\frac{AEV}{\beta}.\int_0^{\psi} \frac{d\left\{\frac{q}{k_s}+e^{\left(-\frac{\psi}{AEV}\right)}\right\}}{\frac{q}{k_s}+e^{\left(-\frac{\psi}{AEV}\right)}} \tag{43}$$

$$-\frac{\beta}{AEV}.z = ln\left[\frac{\frac{q}{k_s}+e^{\left(-\frac{\psi}{AEV}\right)}}{\frac{q}{k_s}+1}\right] \tag{44}$$

Rearranging the above equation could produce the final solution for the suction profile:

$$\psi = \left|-AEV.ln\left[\left(\frac{q}{k_s}+1\right)e^{-\frac{\beta}{AEV}.z} - \frac{q}{k_s}\right]\right| = \left|-AEV.ln\left[\left(\frac{q}{k_s}+1\right)e^{-\frac{\psi_0}{AEV}.\frac{z}{z_u}} - \frac{q}{k_s}\right]\right| \tag{45}$$

To obtain the soil-water characteristic curve equation integrated flow rate, Eq. (45) could be re-substituted into Eq. (35) as follows:

$$S = \frac{C(\psi)}{\left\{ln\left[2.7183+\left(\left|=-AEV.ln\left[\left(\frac{q}{k_s}+1\right)e^{-\frac{\psi_0}{AEV}.\frac{z}{z_u}}-\frac{q}{k_s}\right]\right|/a\right)^n\right]\right\}^m} \tag{46}$$

It should be noted that the initial matric suction of soils at the ground surface is represented by ψ_0. When the measured data for ψ_0 is unavailable, $\psi_0 = \gamma_w.z_u$ might be used as a simplified assumption for hydrostatic conditions according to the suggestion of Lu and Griffiths (2004). Figure 15 displays the flow ratio and matric suction profiles for clays where the matric suction profile is significantly influenced by the steady flow rate.

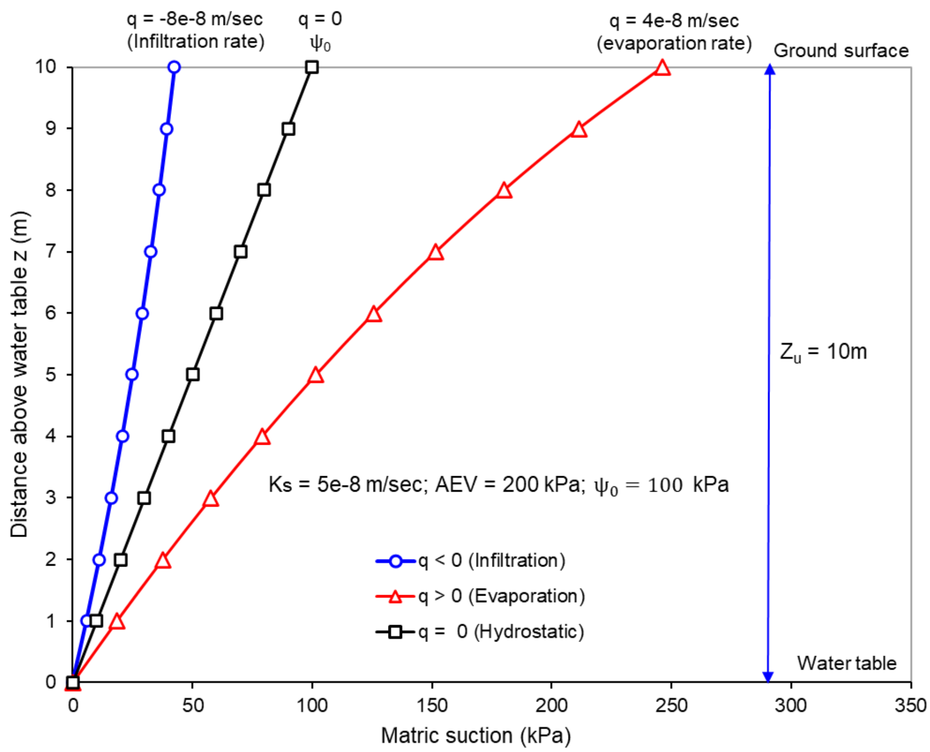

Figure 15. An example of suction profile estimation using analytical equation (Eq. 45)

Ultimate displacement (s_p)

In the proposed model, the slope of the shear stress-displacement curve is controlled by the parameter called ultimate displacement, s_p. Reese (1978) reviewed the relationship between skin resistance and displacement in stiff clays and concluded that the peak displacement, s_p, ranges from about 0.5% to 5% of the pile shaft diameter (d_p). It is noted that the s_p range in sands is comparable to that in clays. Later data (Sharma et al. 1986; Hirayama 1990; Zhang et al. 2010; Pham and Dias 2021b) support the above-mentioned ranges. Judging from the previous studies, the ranges for s_p are as follows:

$$s_p = (0.005 \div 0.05).\, d_p \tag{47}$$

Ultimate disturbance function (D_i^p)

In the proposed interface model, the ultimate disturbance function has a significant impact on the shape of the shear stress-displacement curve. The results of the laboratory tests or a numerical simulation can be used to determine the value D_i^p. According to the results of the direct shear tests, the value D_i^p ranges from about 0.8 to 1 depending on the soil density. In the absence of test results or numerical data, the initial value of the ultimate disturbance function can initially be estimated as follows:

$$D_i^p = \frac{\tau_{cs}}{\tau_p} \tag{48}$$

3.3. Nonlinear model of end-bearing capacity

During installation, the portion of soil immediately below the pile base will be subjected to a compressive axial force and will likely compress in addition to shearing. Shearing is caused by the differences in the vertical and lateral stresses. However, unlike the soil element surrounding the pile shaft, the soil element directly below the base is severely limited. Specifically, the pile weight and the friction force at the pile–soil interface limit any heaving or dilatant response. Additionally, movement is further restricted at the base level by the overburden pressure (vertical effective stress), particularly for long piles. As a result, the pile strain hardens until it reaches the critical state when structural loads are applied. Besides, the field test results also reveal the hardening function of base load displacement (Lee and Park 2008; Seo et al. 2013). This explains why the hardening-strain function (such as hyperbolic) is commonly utilised in analytical approaches and design standards (FHWA-2006, BS8006-2010, Eurocode 7-2013) to simulate the base load-settlement model. In this study, the base load-displacement relationship is modelled by using the hardening function of the proposed interface model as follows:

$$Q_b = q_b.A_b = \left[q_{bu} \left(1 - e^{-\frac{k_{ini}^b}{q_{bu}}.s} \right) \right].A_b \tag{49}$$

where q_{bu} = ultimate unit base resistance, k_{ini}^b = initial compressive stiffness of the soil at the pile base

Ultimate unit base resistance (q_{bu})

There are several methods for calculating the ultimate unit base resistance, one of which makes use of empirical correlation and data from in-situ tests (SPT or CPT). An alternative way is to compute using formulas based on laboratory-tested soil parameters. In the analytical approach presented here, the q_{bu} is calculated by analogy with the bearing capacity of shallow footings and is determined as follows:

$$q_{bu} = \frac{1}{2}\gamma d_p N_\gamma + \sigma'_{zb}.N_q + c'.N_c \tag{50}$$

$$N_q = e^{\pi tan\varphi_b}.tan^2(45^\circ + \varphi_b/2) \tag{51}$$

$$N_c = (N_q - 1).cot\varphi_b \tag{52}$$

where γ = unit weight of soils, σ'_{zb} = vertical effective stress at the pile base, φ_b and c' = internal friction angle and cohesion of soils below the pile base, N_γ, N_q and N_c = bearing capacity coefficients.

For deep foundations with L_p/d_p greater than 5 (L_p being the embedded length of the pile), the first term in Eq. (50) is small compared with the other two terms. It should be noted that the predicted outcome of end-bearing capacity is significantly influenced by the precision of the value N_q. However, when compared to the field N_q values, Eq. (51) frequently overestimates the value N_q, according to several researchers (Coyle and Castello 1981; De Nicola and Randolph 1993; Alawneh et al. 2001; Budhu 2010). This is primarily because the failure mechanism below the pile base might not develop in the same way as that of a shallow foundation due to the considerable overburden pressure acting at the pile base level. In light of the adjusted coefficient, this study suggests the following formula for the factor N_q of the soils at the pile base as follows:

$$(N_q)_{adj} = f_{adj}.e^{\pi tan\varphi_b}.tan^2(45^\circ + \varphi_b/2) \tag{53}$$

$$f_{adj} = \frac{q_{bu}^m}{\sigma'_{zb} + c'.cot\varphi_b}.\frac{1}{e^{\pi tan\varphi_b}.tan^2(45^\circ + \varphi_b/2)} \tag{54}$$

where f_{adj} = adjusted coefficient, q_{bu}^m = measured ultimate unit base resistance

The characteristics of 52 field test projects with measured ultimate unit base resistance are listed in Supplementary Material I along with some brief descriptions. These data sets were collected, which cover a wide variety of possible pile geometry, effective stress, friction angle, and soil types. The scatter in the field data is shown in Figure 16. It is apparent that as the vertical effective stress is increased, the value of f_{adj} decreases. Lower values of f_{adj} denote greater overestimation when applying the conventional theoretical formula (Eq. 51). Although the data sets have not fully converged, the majority of the points appear to follow an exponential relationship. The following formulation is provided for the f_{adj} as an effective stress-dependent function using the regression analysis technique:

$$f_{adj} = e^{-0.006\times\sigma'_z} = \alpha e^{\beta\times\sigma'_z} \tag{55}$$

where α and β = corrected coefficients. When the measured data are known, the corrected coefficients can be derived. Otherwise, the collected data in this study yields the following general statement: α = 1 and $\beta = -0.006$.

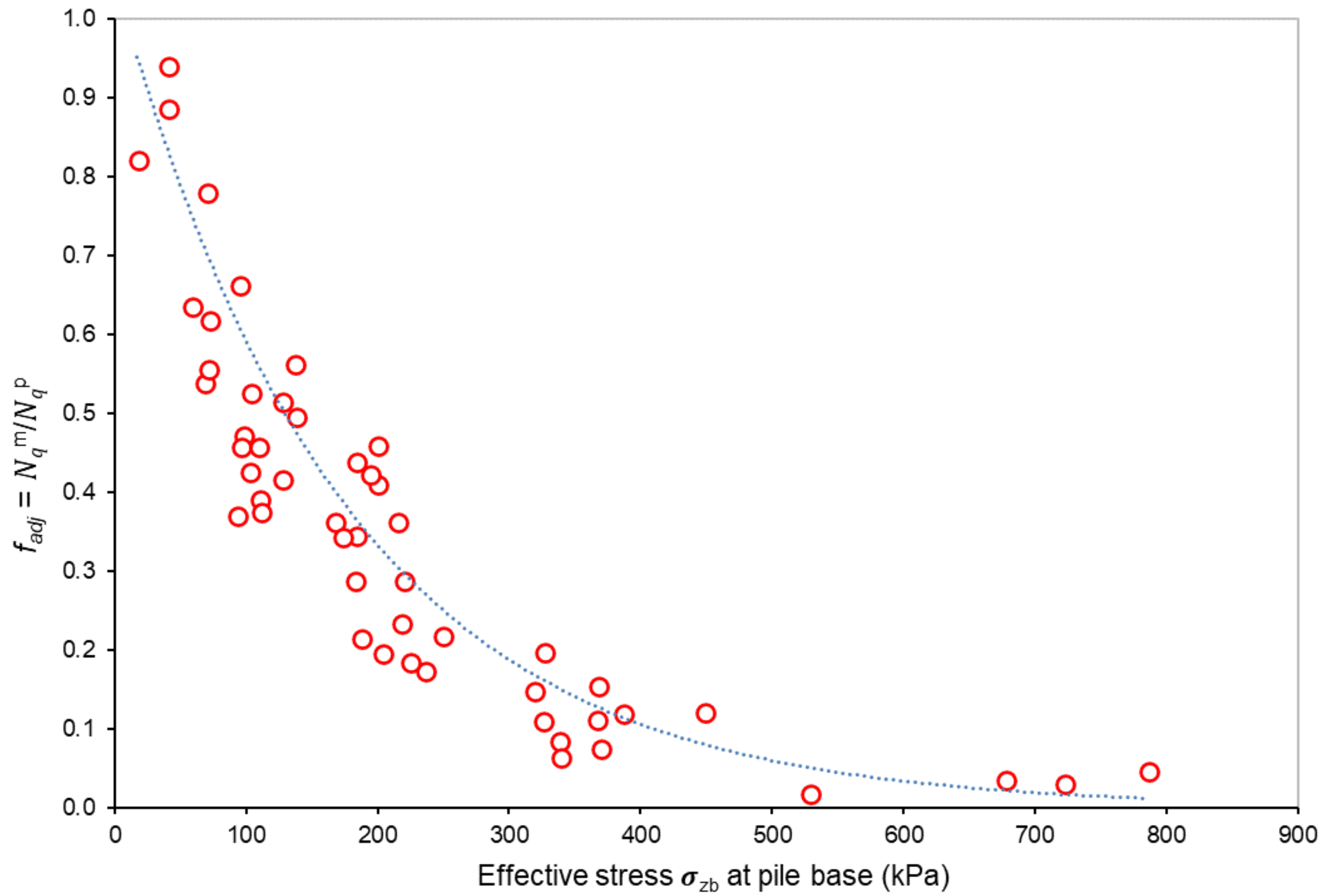

Figure 16. The correlation between the adjusted coefficient and vertical effective stress

Initial elastic soil stiffness (k_{ini}^b)

The initial elastic soil stiffness at the pile base can be determined by relations to ultimate unit base resistance or shear modulus as suggested by Randolph and Wroth (1978) and Pham et al. (2023e):

$$k_{ini}^b = \frac{q_{bu}}{s_p^b} = \frac{4G_{sb}}{\pi r_p(1-\nu_p)} \tag{56}$$

where s_p^b = ultimate displacement, r_p = pile radius, G_{sb} and ν_{sb} = shear modulus and Poisson's ratio of the soil below the pile base, respectively.

3.4. Elastic shortening and distribution of axial force.

The elastic shortening of a pile shaft under load undoubtedly contributes to total settlement at the pile head, particularly in the case of semi-columns. The elastic shortening of a pile depends on the relative development of load transfer between the pile and soil along its length, as well as the load being transferred at the pile base. Because the load transfer is nonlinear and decreases with the depth, the elastic compression of the pile is not uniform. The top of the pile generally experiences greater compression than the bottom. To work out the elastic shortening accurately, an iterative method is required, whereby the pile is divided into elements, and the compatibility of strains is studied at given levels. Figure 17 shows the schematic for force equilibrium analysis on a differential pile element.

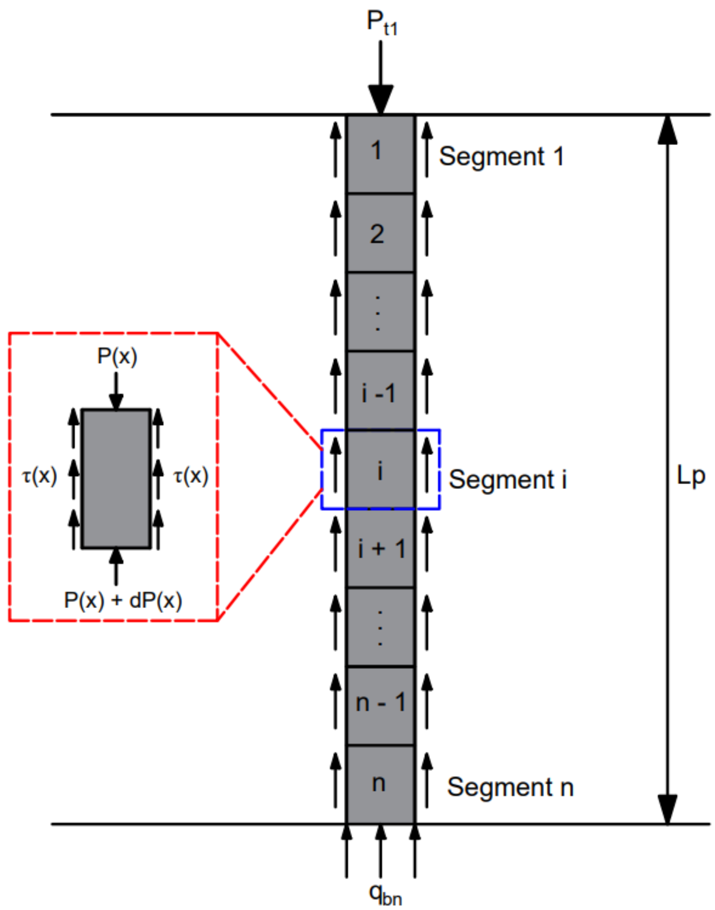

Figure 17. Schematic of typical force equilibrium analysis of pile

As a result of applying static equilibrium to the forces influencing the differential pile element, it provides:

$$dP(x) + C_p\tau(x)dx + A_p q_b(x)dx = 0 \tag{57}$$

where $P(x)$ = axial force in the pile at distance x; C_p = cross-section perimeter of a pile.

It is reasonable to suppose that when loads are applied, the pile is in elastic compression:

$$ds = -\frac{P(x)}{E_p A_p}dx \tag{58}$$

where E_p = elastic modulus of the pile,

Therefore,

$$dP(x) = -E_p A_p \frac{d^2 s(x)}{dx^2} \tag{59}$$

Substituting (59) back into (57) gives:

$$\frac{d^2 s(x)}{dx^2} - \frac{C_p}{E_p A_p}\tau(x)dx - \frac{1}{E_p} q_b(x)dx = 0 \tag{60}$$

By separating the variables, the differential equation can be solved, as

$$\varepsilon(x)\frac{d\varepsilon(x)}{ds} = \frac{d^2 s(x)}{dx^2} \tag{61}$$

By substituting Eq. (61) into Eq. (60) and integrating

$$\varepsilon(x) = \sqrt{\frac{2C_p.b}{E_p A_p}.\left(s + \frac{e^{-as}}{a}\right) + \frac{2C_p.c}{E_p.A_p}\left[\frac{s^3}{3} - \frac{s_p^3}{3}\right] + \frac{2q_{bu}}{E_p}.\left(s + \frac{e^{-k_{ini}^b s/q_{bu}}}{k_{ini}^b/q_{bu}}\right) + C} \tag{62}$$

The boundary condition at the base of the pile can be expressed as:

$$\begin{cases} s\left(x = L_p\right) = s_b \\ \varepsilon\left(x = L_p\right) = 0 \end{cases} \tag{63}$$

Replacing Eq. (63) into Eq. (62) gives the axial strain over the pile length:

$$\varepsilon = \sqrt{\begin{array}{l} \frac{2C_p.b}{E_p A_p}.\left(s + \frac{e^{-as}}{a}\right) + \frac{2C_p.c}{E_p.A_p}\left[\frac{s^3}{3} - \frac{s_p^3}{3}\right] + \frac{2q_{bu}}{E_p}.\left(s + \frac{e^{-\frac{k_{ini}^b s}{q_{bu}}}}{\frac{k_{ini}^b}{q_{bu}}}\right) \\ \quad - \frac{2C_p.b}{E_p A_p}.\left(s_p + \frac{e^{-as_p}}{a}\right) - \frac{2q_{bu}}{E_p}.\left(s_p + \frac{e^{-k_{ini}^b s_p/q_{bu}}}{k_{ini}^b/q_{bu}}\right) \end{array}} \tag{64}$$

3.5. Algorithm for pile load–settlement analysis

Based on the proposed models and the iterative method (Seed and Reese 1957; Lee et al. 2001; Zhang and Zhang 2012), the pile load-settlement response can be obtained. The calculation details are presented with the following procedure, and Figure 18 summarises the algorithm for load-settlement analysis of a single pile embedded in multi-layered soils:

- Step 1. Assume a single pile divided into n segments with a length of $L_i = L_p/n$. The value of n can be specified according to the computational precision demand.
- Step 2. Estimate the ultimate end-bearing capacity by using Eq. (50)
- Step 3. Assume a small pile-base movement, $s = s_{bn}$. Using Eq. (49), calculate the base end-bearing resistance, $Q_b(s)$, caused by the assumed base displacement.
- Step 4. From the proposed load-transfer function as given in Eq. (27), obtain the skin friction resistance at the bottom segment n, $Q_{sn}(s)$, based on the assumed value.
- Step 5. Calculate the total bearing capacity along the pile segment n corresponding to the assumed displacement by: $Q_{tn} = Q_{sn} + Q_{bn}$
- Step 6. Calculate the elastic deformation of the segment as follows, under the assumption that the load in the segment varies linearly:

$$\Delta_n = \left(\frac{Q_{tn} + Q_{bn}}{2}\right)\frac{L_i}{A_p . E_p}$$

- Step 7. Check the elastic deformation of pile segment n within a specified tolerance such as $\Delta_n \leq 10^{-6}\ m$
- Step 8. Calculate the updated midpoint (s'_{cn}) and top (s'_{tn}) displacement of pile segment n given by:

  $s'_{cn} = s_{bn} + \frac{1}{2}\Delta_{sn}$ and $s'_{tn} = s_{bn} + \Delta_{sn}$
- Step 9. Recalculate the skin friction resistance and ultimate bearing capacity of pile segment n based on the updated midpoint displacement.
- Step 10. Repeat steps (4) – (9) for the next segment, and so on, until the value of the load Q_{n1} and displacement s_1 at the pile head are obtained.
- Step 11. Calculate the total skin friction or the sum of the total skin friction capacity and mobilized base capacity.

  $$Q_{t1} = \sum_{i=1}^{n} Q_{si} + Q_{bn}$$
- Step 12. Calculate the axial strain of the pile corresponding to the assumed displacement by using Eq. (64)
- Step 13. Repeat the procedure from steps (3) through (12) using different assumptions for the settlement at the pile base in order to get a series of load-displacement values. The proposed method might be used to determine the load-settlement curve, skin friction distribution along the pile depth, and the distribution of axial loads along the pile.

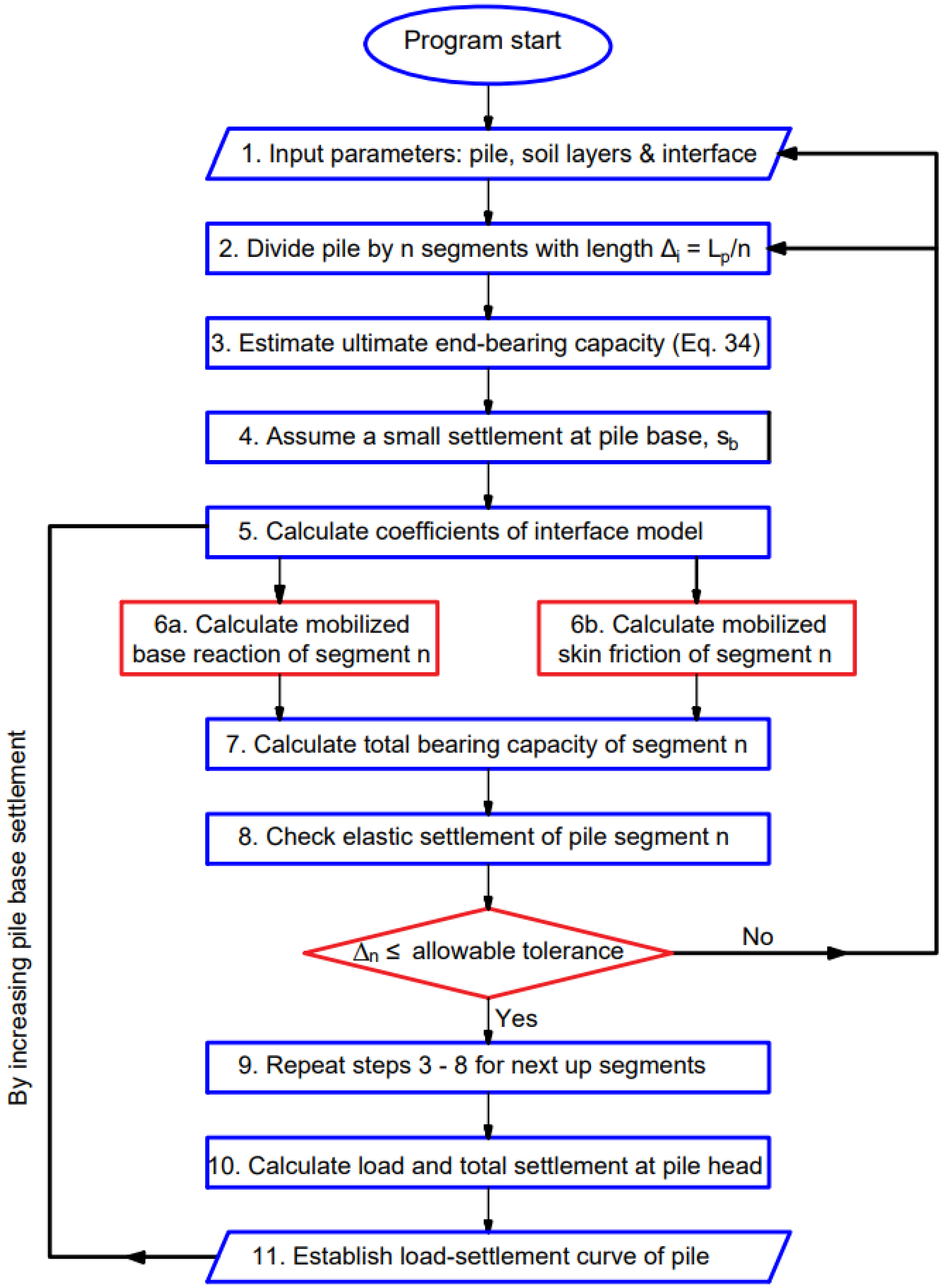

Figure 18. Flow chart for load-settlement response analysis of piles

3.6. Discussion of the analytical method

Three factors are crucial for numerical simulations of a geostructure to perform well, which include the input parameter quality, the soil model that was used, and the loading simulation process. First, it should be noted that neither sophisticated nor basic models—such as Mohr-coulomb or elastoplastic—can replicate the deterioration of skin friction at the soil-structure interface. In order to get beyond the limitations of the models that are currently accessible, the DSC-based interface model that was described in this study could be taken into consideration as a choice to be implemented into numerical software. This work also discusses the profile of steady-state in-situ matric suction, soil-water characteristic curve, and pore-water pressure of unsaturated soils that allows to application of the proposed method to piles in unsaturated soils.

Additionally, it is noted that the proposed analysis method in this study only needs a few basic soil-pile interface input parameters, similar to current design methods that include friction angle, cohesion, interaction coefficient, and disturbance degree of soils corresponding to peak shear strength and displacements. Specifically, it is assumed that the displacement parameter (s_p) are proportionate to pile size. Two shear strength parameters (τ_{cs}, τ_p) are derived from friction angles and cohesion in the same way as other models. And governing coefficients (a, b, c) are computed directly from the aforementioned parameters. It appears that, in comparison to previous models, the current approach does not introduce extra parameters while still being able to accurately characterize the hardening-softening behaviour of the soil-structure interface.

Evidently, the quality of these input parameters has a significant impact on the performance of the method. Within this framework, the experimental data may improve the input parameter's reliability and hence contribute to the production of a better prediction. To obtain these parameters, there are a few potential approaches that might be used such as i) carrying out tests on model-scale piles, ii) carrying out interface shear tests in a laboratory, iii) utilizing on-site CPT/SPT data, and iv) performing field tests and back analysis approaches. In terms of economy, the interface shear tests, and model-scale tests may theoretically be the most suitable option. Following that, an analytical method will be employed to use the input parameters derived from the interface shear tests and model-scale tests to simulate the outcomes of field tests. The main difficulty in performing model-scale tests or laboratory tests, nevertheless, is making sure the model pile's condition is precisely the same as the in-situ pile (in terms of scaling effects).

On the other hand, the analytical solutions in this work could be applied as an independent analytical approach that does not necessitate integration with numerical techniques. For design engineers, this offers an efficient and straightforward option, particularly during the preliminary design stage. For example, the analytical solutions could likewise be computed automatically by creating spreadsheets or MATLAB code. Compared to performing a numerical simulation, this saves far too much effort and time. In particular, for rigid pile (elastic settlement), it is simple to get the solution of the developed method and there is no need to use trial values to get the solution of unknown parameters.

Finally, simulating the impact of pile installation and surrounding soil disturbance in current numerical models is a significant issue. The DSC-based analytical solutions may offer an additional method to account for this effect. The proposed approach might be used to anticipate any kind of soil rather than being limited to a specific soil type as an empirical model. The proposed analytical approach may be helpful not only for forecasting the load-settlement of a pile using input parameters but also for optimizing design and organizing a suitable loading-test programme.

4. Performance of the proposed method in comparison to field measurements

The effectiveness of the proposed framework is assessed by comparing the predicted results with those deduced from field experiments on a single pile. To demonstrate the implementation of the proposed approach in a variety of ground conditions and pile types, the following five projects with well-documented sources have been chosen from the database of static load tests on piles. As previously mentioned, there are different ways to obtain model calibration parameters such as using interface shear tests, model tests or on-site CPT/SPT results. However, it is hard to find a case that offers both results of full-scale field tests and interface shear tests. This could be the result of the difficulty in preparing soil samples for interface shear experiments that have physical characteristics and disturbances comparable to the actual soil conditions. A case study was recently reported by Feng et al. (2024) that presents the results of interface shear and field tests, which are used to demonstrate how the model is calibrated using interface shear testing. In the case of the remaining four examples, input data points were gathered directly from site records (SPT or CPT) due to the interface shear test results not being presented in the original papers. The evaluation of soil shear strength characteristics, including internal friction angle, cohesion and shear modulus, can be achieved using laboratory test results or empirical correlations with SPT blow counts. A list of these relationships is given in Appendix II. In this study, the shear strength properties were derived from SPT blow counts in the absence of laboratory test data using the equation suggested by Hettiarachchi and Brown (2009). The model calibration parameters for the Feng et al. (2024) example obtained via interface shear testing are shown in Table 2, while the model calibration parameters for all other cases identified via on-site SPT/CPT are shown in Table 3.

It should be mentioned that in the first project (Feng et al. 2024), second project (Caputo et al. 1991) and third project (Lee et al. 2003), the soil layers were presumed to be saturated as the groundwater table was located near the ground surface. The last two examples (Fellenius et al. 2004; Lee and Park 2008), however, described that the groundwater table emerged at a specific depth and the soil layers above became unsaturated. The fundamental steps for determining the load-settlement curve of the pile using the proposed method could be summarized as follows:

Step 1. Employing the results of interface shear tests for model calibration, if available, or using the SPT or CPT data to infer the shear strength parameters, such as friction angle, cohesion, undrained shear strength, and modulus.

Step 2. Estimation of peak and critical state skin friction of pile-soil interface (eq. 28) as well as ultimate bearing capacity of soil at pile base (eq. 50)

Step 3. Determine parameter s_p by using eq. (47) or by interface shear test results if data is available.

Step 4. Calculate the peak disturbance function by using eq. (48) where $D_i^p = \tau_{cs}/\tau_p$ or by interface shear test results if data is available.

Step 5. Calculate the calibration parameters a, b, c by using eqs. (19), (21), (25)

Step 6. Establish transfer functions for pile shaft (eq. 27) and pile base (eq. 49)

Step 7. Estimate the load-settlement curve.

Step 8. Estimate the axial strain and elastic shortening for semi-columns (eq. 64), or neglect for rigid piles.

Table 2. Summary of model parameters obtained via on-site CPT/SPT for case of Feng et al. (2024).

Parameters	Layer 1 – silty clay	Layer 2 – silty sand	Layer 3 – muddy clay	Layer 4 – Clay	Layer 5 – silty clay	Layer 6 – sandy silt
Soil layer thickness t_i (m)	3.6	5.4	3.0	6.0	12.0	22.0
Unit weight γ (kN/m^3)	18.9	19.9	18.8	17.4	17.3	19.3
Initial shear stiffness k_{ini} (kPa/m)	100	120	180	290	420	-
Ultimate disturbance D_i^p $(dimensionless)$	0.99	0.96	0.99	0.99	0.94	-
Peak shear stress τ_p (kPa)	32	61	108	170	300	-
Ultimate displacement s_p (m)	0.003	0.003	0.003	0.003	0.003	-
Internal friction angle φ' (°)	28.5	27.4	26.3	23.1	30.1	32.0
Effective cohesion c' (kPa)	4.0	4.6	0	12.0	4.7	2.0

Table 3. Summary of four field test datasets with model parameters obtained via on-site CPT/SPT

Field test projects	Pile geometry	Soil layer 1	Soil layer 2	Soil layer at base
Caputo et al. (1991)	$d_p = 1.5m$ $L_p = 42m$ $E_p = 50\ GPa$	Saturated organic silt (32m) $\gamma = 12\ kN/m^3$ $\varphi_p = 24$ (preliminary) $\varphi_p = 26.7$ (back analysis) $D_i^p = 0.995$ $S_p = 0.02\ m$ $S = 100\%$ (saturation degree)	Saturated silty sand (8m) $\gamma = 16\ kN/m^3$ $\varphi_p = 36$ (preliminary) $\varphi_p = 33.4$ (back analysis) $D_i^p = 0.990$ $S_p = 0.02\ m$ $S = 100\%$ (saturation degree)	Saturated indurated pozzolana $\gamma = 17.5\ kN/m^3$ $\varphi_p = 30.6$ (preliminary) $\varphi_p = 28.5$ (back analysis) $k_{ini}^b = 700$ (preliminary) $k_{ini}^b = 750$ (back analysis)
Lee et al. (2003)	$d_p = 0.356m$ $L_p = 8.24m$ $E_p = 50\ GPa$	Saturated loose sand (3m) $\gamma = 17.5\ kN/m^3$ $\varphi_p = 33$ (preliminary) $\varphi_p = 33.0$ (back analysis) $D_i^p = 0.991$ $S_p = 0.06\ m$ $S = 100\%$ (saturation degree)	Saturated dense sand (5m) $\gamma = 17.5\ kN/m^3$ $\varphi_p = 40$ (preliminary) $\varphi_p = 38.6$ (back analysis) $D_i^p = 0.980$ $S_p = 0.06\ m$ $S = 100\%$ (saturation degree)	Saturated gravelly sand $\gamma = 17.5\ kN/m^3$ $\varphi_p = 46.3$ (preliminary) $\varphi_p = 44.2$ (back analysis) $k_{ini}^b = 300$ (preliminary) $k_{ini}^b = 350$ (back analysis)
Fellenius et al. (2004)	$d_p = 0.406m$ $L_p = 45m$ $E_p = 50\ GPa$	Sandy silt (3m was unsaturated soil and 6m was saturated soil) $\gamma = 17.9\ kN/m^3$ $\varphi_p = 25.8$ (preliminary) $\varphi_p = 28.2$ (back analysis) $D_i^p = 0.995$ $S_p = 0.01\ m$ $S = 60\%$ (saturation degree)	Saturated soft clay (39m) $\gamma = 17.4\ kN/m^3$ $\varphi_p = 15$ (preliminary) $\varphi_p = 18.6$ (back analysis) $D_i^p = 0.985$ $S_p = 0.01\ m$ $S = 100\%$ (saturation degree)	Saturated soft clay $\gamma = 17.4\ kN/m^3$ $\varphi_p = 30.9$ (preliminary) $\varphi_p = 27.5$ (back analysis) $k_{ini}^b = 30000$ (preliminary) $k_{ini}^b = 50000$ (back analysis)
Lee and Park (2008)	$d_p = 1.2m$ $L_p = 37.4m$ $E_p = 50\ GPa$	Silty clay (8m was unsaturated and 10.5m was saturated soil) $\gamma = 17.5\ kN/m^3$ $\varphi_p = 32.5$ (preliminary) $\varphi_p = 32$ (back analysis) $D_i^p = 0.99$ $S_p = 0.05\ m$ $S = 72\%$ (saturation degree)	Saturated clayey silt (18.5m) $\gamma = 15\ kN/m^3$ $\varphi_p = 25$ (preliminary) $\varphi_p = 29.2$ (back analysis) $D_i^p = 0.99$ $S_p = 0.05\ m$ $S = 100\%$ (saturation degree)	Saturated very stiff clay $\gamma = 16\ kN/m^3$ $\varphi_p = 30$ (preliminary) $\varphi_p = 31$ (back analysis) $k_{ini}^b = 40000$ (preliminary) $k_{ini}^b = 100000$ (back analysis)

It should be highlighted that the effectiveness of the analytical method depends significantly on the quality of the input parameters. Laboratory tests, such as direct shear tests or triaxial tests, can be employed to determine the model parameters. Many complex aspects, including construction techniques, pile types, soil types, and loading techniques, have an impact on the interface behaviour of an actual pile at the site. It is generally known that, after pile installation, the in-situ state of the soil around the pile shaft is significantly altered. It is very difficult to simulate the state of the soil after pile installation. For a driven pile, the radial stress generated around the pile shaft is uncertain, while the interface roughness between the pile shaft and surrounding soil is unknown for a bored pile. Therefore, the magnitude of the resulting input parameters will be significantly impacted by these considerations. A back-analysis methodology is an additional approach to determine these input parameters in order to take into account input parameter uncertainty and support optimization design. As a result, three cases are considered for comparison in this study: (1) preliminary prediction without using adjusted N_q factor (Eq. 51); (2) preliminary prediction using adjusted N_q factor (Eq. 53); (3) prediction using back analysis-based input parameters.

4.1. Field measurement of bored piles in Shanghai, China

A compelling example, recently described by Feng et al. (2024), was the application of both laboratory interface shear experiments and full-scale field tests to piles. This enables us to illustrate predicting the load-settlement response of piles based on the input parameters acquired from interface shear tests. The test bored pile was 30m long with an outer diameter of 0.6m. The geological conditions of the test pile are typical of a soft soil area, filled with silty clay and sandy silt, and clay from top to bottom, as shown in Figure 19a. It should be noted that the shear strength characteristics of each soil layer were obtained from the interface shear tests. Figure 19b shows the relationship between the shear stress and the relative displacement, which was obtained from the direct shear test results on the interface between the concrete and the five typical soils at the pile depth. A similar pattern was observed in the changes in the interface shear stresses for different soil samples during the shear tests. The proposed skin friction model takes into account four important parameters: ultimate disturbance function (D_i^p), displacement corresponding to peak shear stress (s_p), peak shear stress (τ_p), and initial shear stiffness (k_{ini}). The initial shear stiffness might be determined by calculating the slope of the tangential line on the curve during the first segment. The test results (marker) and the predicted curve (solid line) created by the proposed model agree quite well. This means that the relationship between interface shear stress and displacement has been accurately captured by the suggested method given in section 2.2. These calibration model parameters are then used to predict the load-settlement curve of piles in situ. The load-displacement curves of the test piles under variable mechanical loads are shown in Figure 19c. The success of the proposed framework was confirmed when it was found that the load-transfer method suggested in this study more correctly represented the overall trend of the measured values. Additionally, it was noted that the end-bearing resistance has a nonlinear hardening tendency while the average skin friction resistance exhibits a nonlinear softening behaviour. At small settlements, the skin friction component is observed to mobilise more quickly than the end-bearing component, but it reduces after attaining the ultimate value.

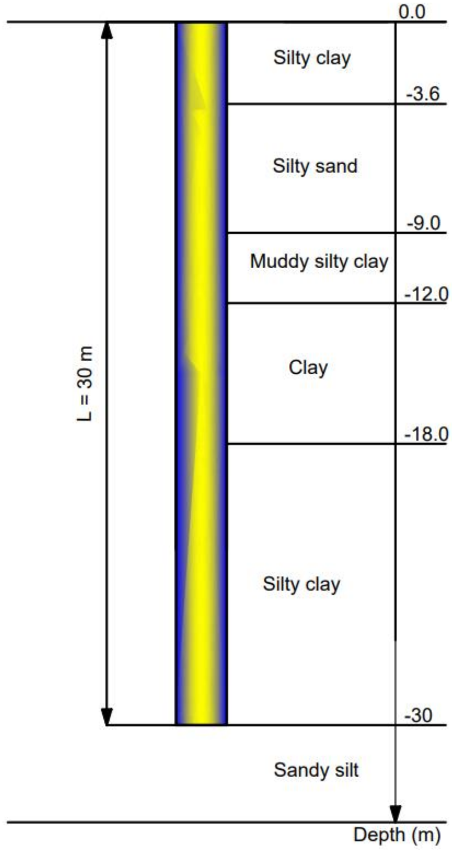
0.0
Silty clay
-3.6
Silty sand
-9.0
Muddy silty clay
-12.0
Clay
-18.0
Silty clay
-30
Sandy silt
L = 30 m
Depth (m)

a)

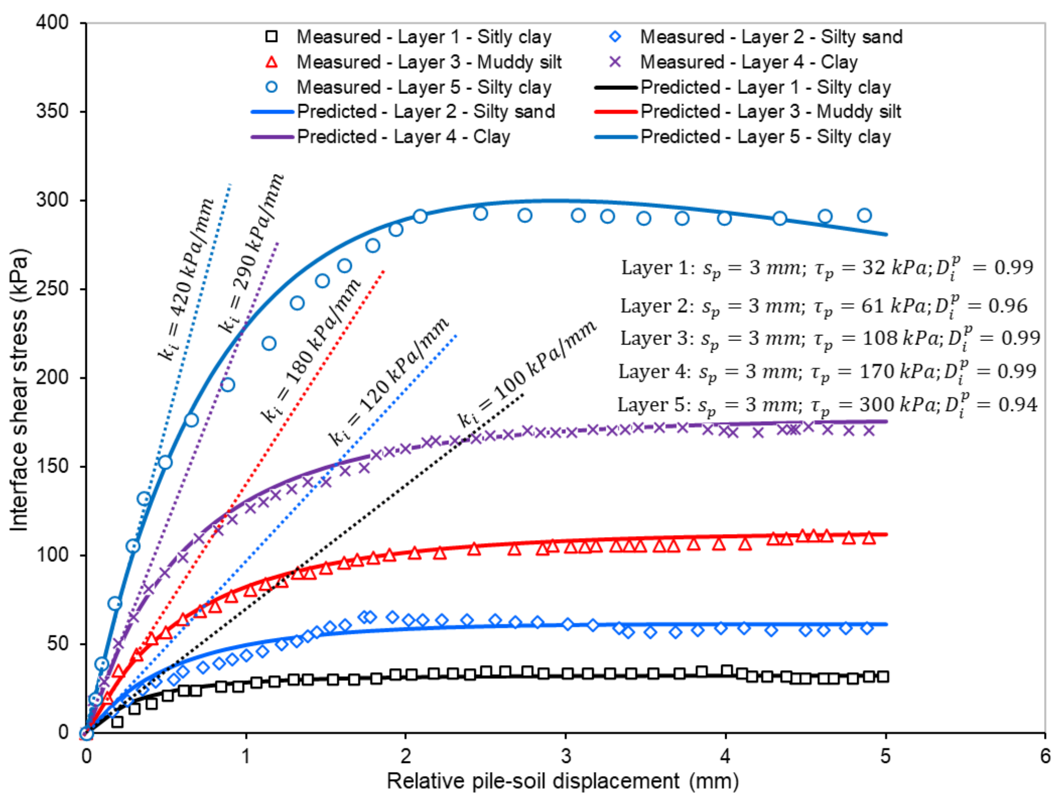
Measured - Layer 1 - Sitly clay
Measured - Layer 2 - Silty sand
Measured - Layer 3 - Muddy silt
Measured - Layer 4 - Clay
Measured - Layer 5 - Silty clay
Predicted - Layer 1 - Silty clay
Predicted - Layer 2 - Silty sand
Predicted - Layer 3 - Muddy silt
Predicted - Layer 4 - Clay
Predicted - Layer 5 - Silty clay
$k_i = 420\ kPa/mm$
$k_i = 290\ kPa/mm$
$k_i = 180\ kPa/mm$
$k_i = 120\ kPa/mm$
$k_i = 100\ kPa/mm$
Layer 1: $s_p = 3\ mm;\ \tau_p = 32\ kPa; D_i^p = 0.99$
Layer 2: $s_p = 3\ mm;\ \tau_p = 61\ kPa; D_i^p = 0.96$
Layer 3: $s_p = 3\ mm;\ \tau_p = 108\ kPa; D_i^p = 0.99$
Layer 4: $s_p = 3\ mm;\ \tau_p = 170\ kPa; D_i^p = 0.99$
Layer 5: $s_p = 3\ mm;\ \tau_p = 300\ kPa; D_i^p = 0.94$
Interface shear stress (kPa)
Relative pile-soil displacement (mm)
0
50
100
150
200
250
300
350
400
1
2
3
4
5
6

b)

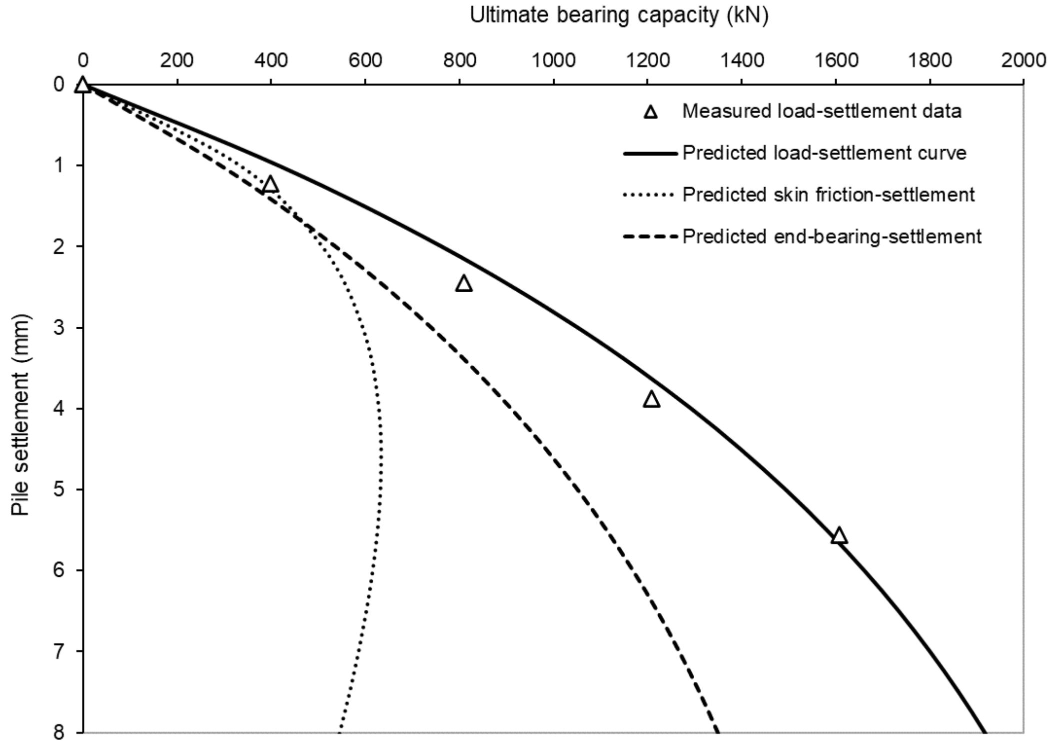

c)

Figure 19. Comparison of predicted and measured results for test pile in Shanghai (test data after Feng et al. 2024): a) pile test profile, b) interface shear test results, c) load-settlement curve

4.2. Field measurement of bored piles in Naples, Italy

Caputo et al. (1991) performed static load tests on two piles with different diameters. Both test piles were 42 m long, but one was 1.5 m, and the other was 2 m in diameter. This project is an interesting illustration of the advantages of the back analysis procedure, due to having piles with different geometries. Figure 20a shows the profile of the test pile and soil conditions. The piles penetrate through the relatively weak soil layers, which are buried in 32 m of organic silt and 8 m of pozzolana. The ultimate resistance is frequently promptly mobilized at a small settlement due to the characteristic of soft soil, and the degradation then happens quickly after that. Figure 20b demonstrates the mobilization of skin friction resistance with pile settlement for various soil layers, where the hardening-softening behaviour was seen in the curves of three different soil layers. Each skin friction curve in this figure represents the skin friction capacity of a single layer and the total skin friction capacity of all soil layers where the pile penetrated through. The ultimate skin friction resistance often peaks at a settlement of 18 mm ($\approx 0.012\ d_p$). The comparison of the end-bearing resistance and skin friction resistance curves is shown in Figure 20c. Although it seems that skin friction is smaller than the end-bearing resistance, this difference is dependent on the mobilized settlement. For instance, the skin friction resistance is less than the end-bearing resistance by around 13.6% at the peak state and 45.6% at the residual state.

The comparison of the load-settlement curves for ultimate bearing capacity for predicted and measured data is shown in Figure 20d. It should be observed that as pile settlement increases, the ultimate bearing capacity rises and peaks at 35 mm ($\approx 0.023\ d_p$) before decreasing. The comparative findings demonstrate that the black dot line, which represents the curves predicted using the back-analysis approach has the best fit with the measured curve. Curves predicted with input parameters based on SPT/CPT, on the other hand, have a greater error but still exhibit good agreement with the measured one (red solid curves). It should be stressed that, as previously indicated, there are a number of complex aspects that could affect the production of a prediction curve and it would be very difficult to match perfectly with the measured curve while using input parameters obtained from laboratory tests or CPT. Specifically, The average relative error is only 2.2% for the prediction case utilizing input parameters based on back analysis, 7.9% for the prediction case using CPT-based model calibration as well as an adjusted factor, and 12.7% for the prediction case using CPT-based model calibration without an adjusted factor. The ultimate bearing capacity of the test pile with a 2 m diameter is then predicted using the input parameters derived from the back analysis technique for the test pile with a 1.5 m diameter. It should be highlighted that for the test pile with a diameter of 2 m, an excellent match between the analytical and experimental curves is seen with a relative error of approximately 5.3%, demonstrating the robust estimation capabilities of the proposed model (Figure 20e).

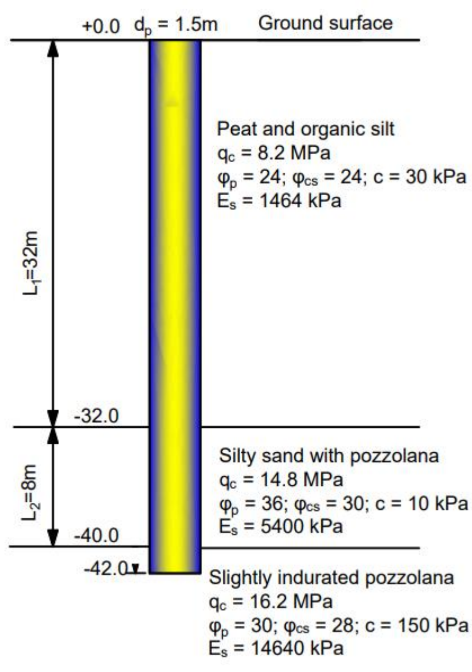

a)

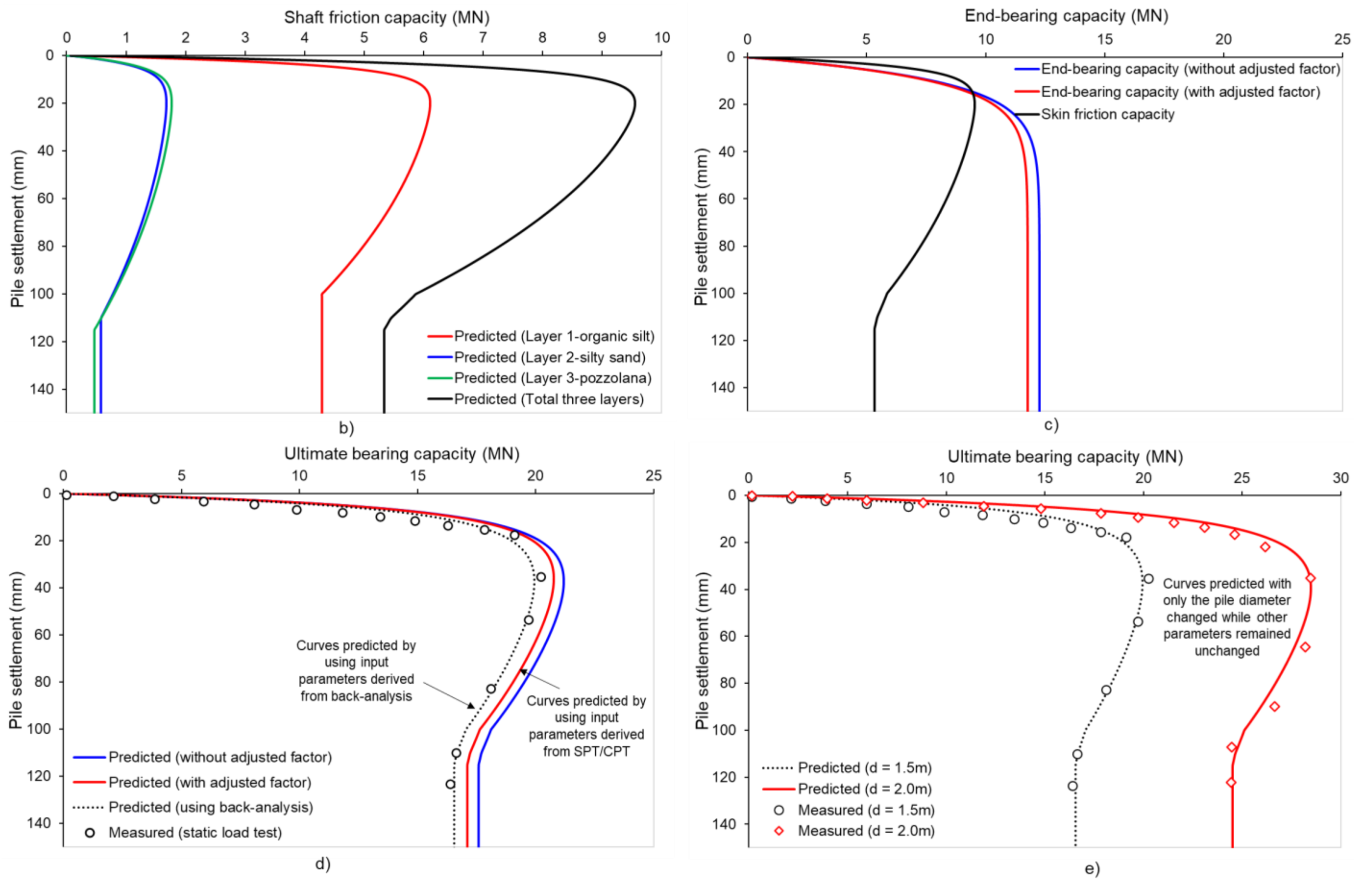

Figure 20. Comparison of predicted and measured results for test pile in Italy (data after Caputo et al. 1991): a) pile test profile, b) skin friction capacity, c) end-bearing capacity, d) ultimate bearing capacity for pile with a diameter of 1.5m, e) ultimate bearing capacity for pile with a diameter of 2m

4.3. Field measurement of pipe piles in LaGrange, Indiana

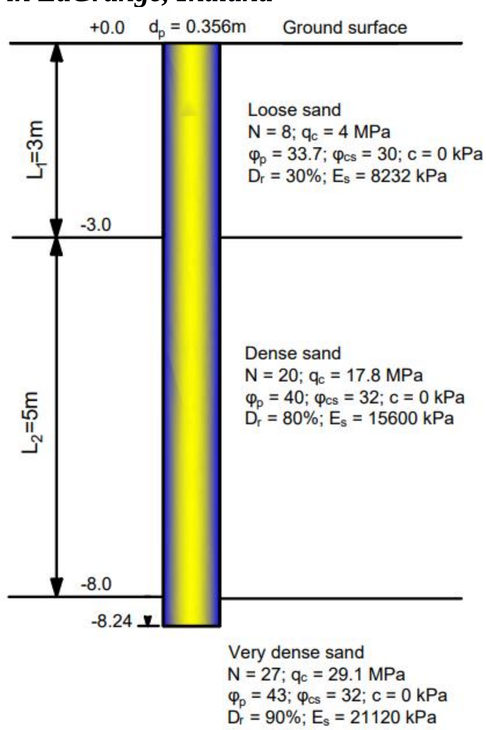

a)

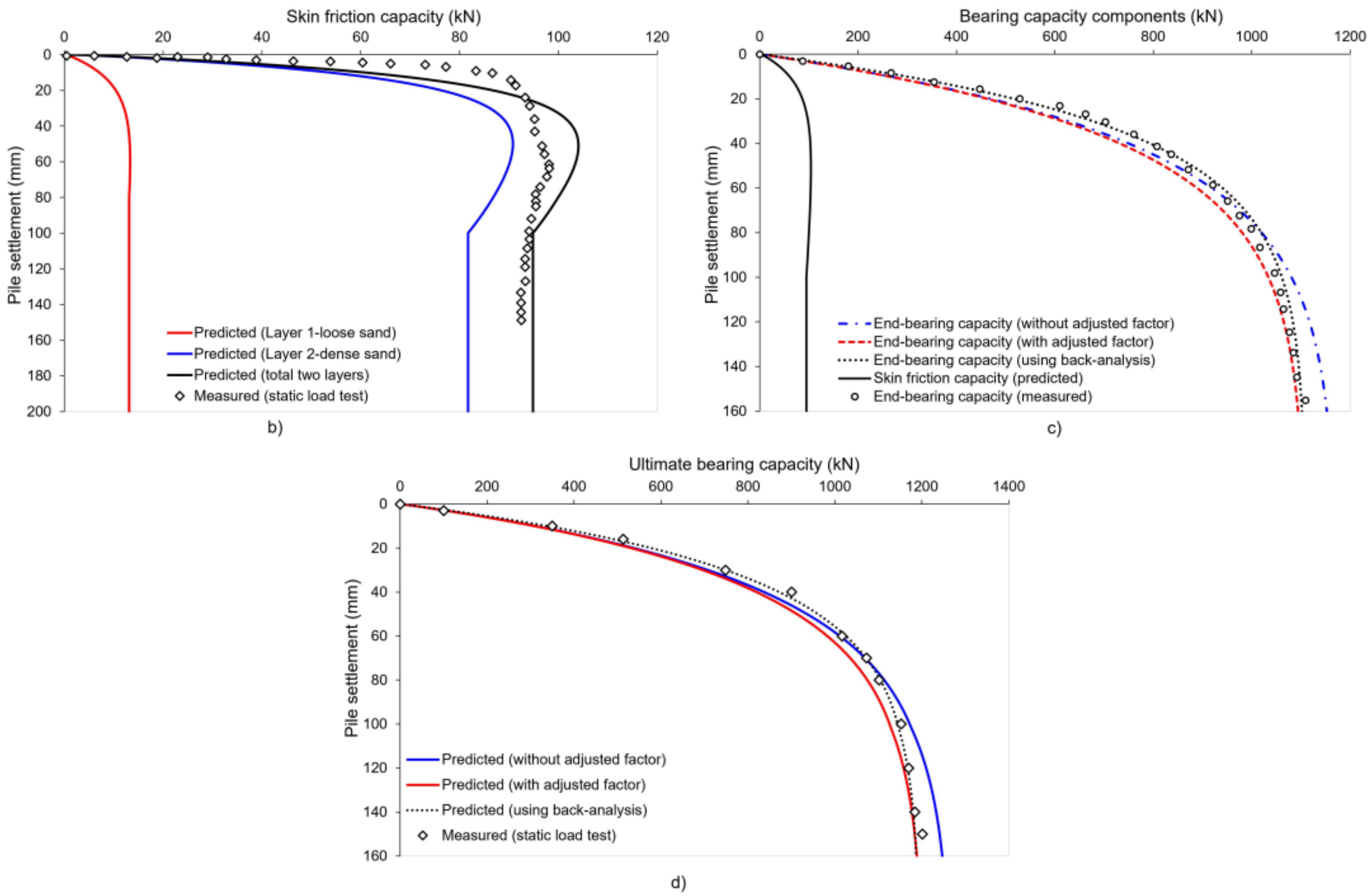

Figure 21. Comparison of predicted and measured results for test pile in Indiana (data after Lee et al. 2003): a) pile test profile, b) skin friction capacity, c) end-bearing capacity, d) ultimate bearing capacity

The load capacity of both closed- and open-ended piles are reported by Lee et al. (2003) through an experimental programme utilizing calibration chamber model pile load tests and field pile load tests. The test site is close to the Han River in Indiana. Due to the characteristics of test pipe piles penetrating sand layers of varying densities, this project is chosen for performance analysis. Moreover, the measured skin friction and end-bearing capacity of piles are separately provided, which is beneficial for comparison. The profile of the test pile and the soil conditions are shown in Figure 21a. As can be observed, the soil site is primarily loose, gravelly sand deposit with a $D_r = 30\%$ up to a depth of 3 meters. Conditions are dense to very dense throughout the rest of the sand deposit, which is down to a depth of 13–14 m ($D_r = 80\%$). Figures 21b and 21c, respectively, show the results of the resistance analysis of the components that include skin friction and end-bearing. The measured data reveals that while the end-bearing resistance only exhibits hardening behaviour, the skin friction resistance exhibits a softening behaviour after reaching its maximum value at a settlement of 18 mm ($\approx 0.05\ d_p$). In this instance, the end-bearing component has a significantly higher contribution to the ultimate bearing capacity compared to the skin friction. It is important to note that a variety of complex factors, including the soil characteristics, loading procedure, and construction technique, can affect how a real pile behaves at the interface, which accounts for the difference between the expected and actual curves (Fig. 21b). The pile length in this example was only 8 m, with 3 m in loose sand and 5m in dense sand. Because of pile construction, soil recovery, and contact damage between the soil and structure for shallow layers, the mobilisation of shaft friction would be greatly impacted. Consequently, fitting the skin friction-settlement curve appropriately would be challenging in this scenario. More importantly, though, is that the softening tendency of the friction shaft components is found to be appropriately predicted by the analytical model. As a result, it could be concluded that the proposed model still provides a potential choice for the load-settlement analysis of piles. Concerning modelling the load-settlement response of both resistance components, the predicted curves and the measured one agree well. The comparison of the predicted and measured curves for the ultimate bearing capacity of piles is shown in Figure 21d. It is noted that there is good agreement between curves derived using the analytical model and field measurements. Using the back analysis-based input parameters enhanced the performance of the proposed model. The average relative error for the prediction case that used input parameters based on back analysis was 3.4%, for the prediction case with CPT-based model calibration that used an adjusted factor was 8.7%, and for the prediction case with CPT-based model calibration that did not use an adjusted factor was 15.1%.

4.4. Field measurement of the driven pile in Sandpoint, Idaho

Fellenius et al. (2004) provide the results of a static load test on a driven pile with a diameter of 0.406 m which was driven to a depth of 45 m on soft, compressible soil. The profile consists of a layer of sandy and silty soil roughly 6 m thick and a layer of clay measuring roughly 40 meters. Unlike other projects, the pile base in this case is supported by soft clay. Thus, it is anticipated that the skin friction resistance will significantly contribute to the ultimate bearing capacity of the pile. In addition, the groundwater table was discovered at a depth of 3 m below the ground surface. Therefore, the sandy silt layer could be separated into 3m of unsaturated soil with a 60% saturation degree, and the remaining 6m were accepted to be saturated. Since the measured soil-water characteristic curve was not provided, the suction profile is predicted using Equation (45) with a flow rate of 1.15e-9 m/s as demonstrated in Figure 22a. Figures 22b and 22c show the mobilization of skin friction resistance and end-bearing resistance of the considered pile, respectively. It should be noted that because the pile has a long length and its base rests on soft soils, skin friction accounts for around 80% of the total bearing capacity and is more than four times the end-bearing resistance. As a result, the test pile is classified as a friction pile. The comparison of the predicted and measured load-settlement curves is shown in Figure 22d. It is noted that the analytical model predicts the load-settlement response with good agreement to measurements. The average relative error is 5.6% in the prediction case using input parameters based on back analysis, 14.5% in the prediction case with CPT-based model calibration using an adjusted factor, and 16.1% in the scenario without an adjusted factor. Moreover, the data from static load tests show that as settlement increases, the ultimate bearing capacity increases as well, and then exhibits softening behaviour after reaching the ultimate value. A reason for the softening response in this situation can be attributed to the interface between soft clay and the pile, which is frequently destroyed at a small displacement, resulting in a reduction in skin friction resistance.

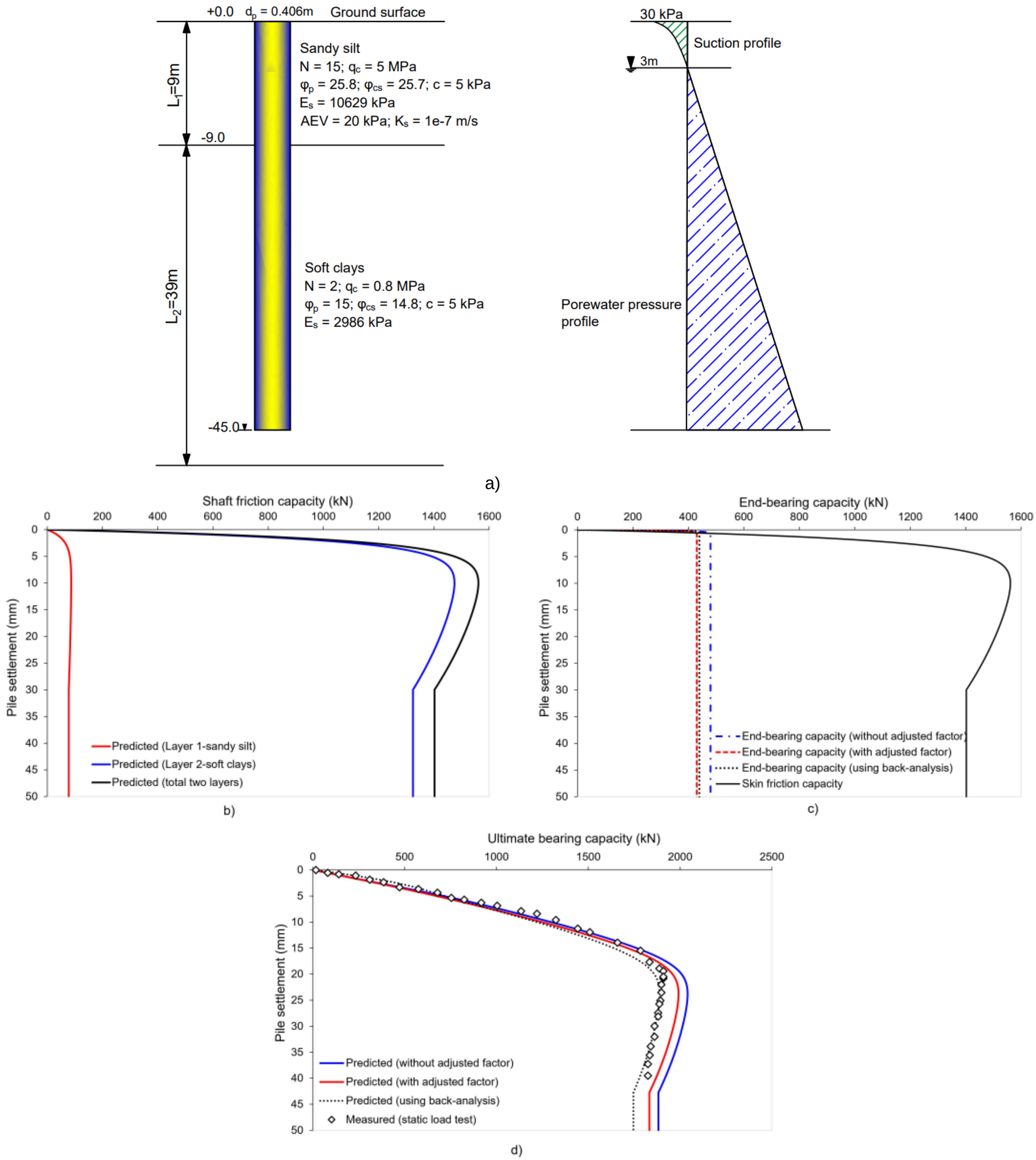

Figure 22. Comparison of predicted and measured results for test pile in Idaho (data after Fellenius et al. 2004): a) pile test profile, b) skin friction capacity, c) End-bearing capacity, d) ultimate bearing capacity

4.5. Field measurement of the bored pile in Singapore

The field measurement results on a bored pile with a diameter of 1.2 metres and a length of 37.4 metres were reported by Lee and Park (2008). Having results from both the O-cell test and the static load test, the project is an important one for comparison purposes. It should be emphasised that because the pile is regarded as a wholly rigid entity in the theory of the O-cell test, the elastic settlement of piles is negligible. However, the pile practically suffers elastic shortening with an applied load, and its strain decreases with depth. Due to this advantage, the results of static load testing are used as a benchmark for comparison, while the results of O-cell tests are only used to examine the behaviour of the load-settlement curves of the resistance components. The test piles and soil profile are shown in Figure 23a. It was found that the test pile penetrated through layers of silty clay and had toe bearing from the very stiff/stiff silty clay. Because the groundwater table was discovered at a depth of 8m below the ground surface, the silty clay layer could be separated into 8m of unsaturated soil with a 72% saturation degree, and the remaining 10.5m were taken to be saturated. It would be ideal to obtain SWCC data at various depths because the flow rate varies with depth. Unfortunately, the original article did not include the SWCC data. As a result, the authors cite the SWCC data of silty clay with similar physical properties that were reported by Uchaipichat and Khalili (2009). The SWCC utilised to determine the AEV, matric suction, and corresponding degree of saturation is shown in Figure 22b. An example for estimating the confining pressure of unsaturated soils at the ground surface is illustrated here. In this case, the effective pressure of unsaturated soil at the ground surface would be $(\sigma_v')_{unsat} = (u_a - u_w).S_e = 80x0.72 = 57.6\ kPa$. The earth pressure coefficient $K_{E=}\ (1 - sin\varphi_{cs}).(OCR)^{0.5}.tan(R_i.\varphi_{cs}) \approx 0.26$. The confining pressure at the ground surface will be $(\sigma_h')_{unsat} = (u_a - u_w).S_e.K_E = 80x0.12x0.26 = 15\ kPa$

Figures 23c and 23d show the prediction outcomes for the skin friction capacity and end-bearing capacity, respectively. It is discovered that, while the end-bearing capacity constantly increases nonlinearly with settlement, the skin friction capacity increasingly mobilises with pile settlement and approaches a limiting value at 15.5mm ($\approx 0.013\ d_p$). Moreover, the skin friction component contributes significantly more to the overall bearing capacity of the pile than its end-bearing capacity does. Figure 23e compares the results of predictions and measurements for ultimate bearing capacity. It is evident that the shapes of the predicted and measured curves are quite comparable. With a relative error of roughly 7.2%, the load-settlement response derived from the analytical model consistently agrees with that of static load tests. Also, it was discovered that the predicted curve with input parameters based on back analysis had a greater agreement with the measured curve, indicating that the proposed model's performance may be enhanced by increasing the accuracy of the input parameters. In comparison to static load tests, the results of the O-cell test were likewise shown to be overestimated. This is considered to be due to the elastic shortening of the pile not taken into account by the O-cells, which only assessed the relative displacement between the soils and the pile.

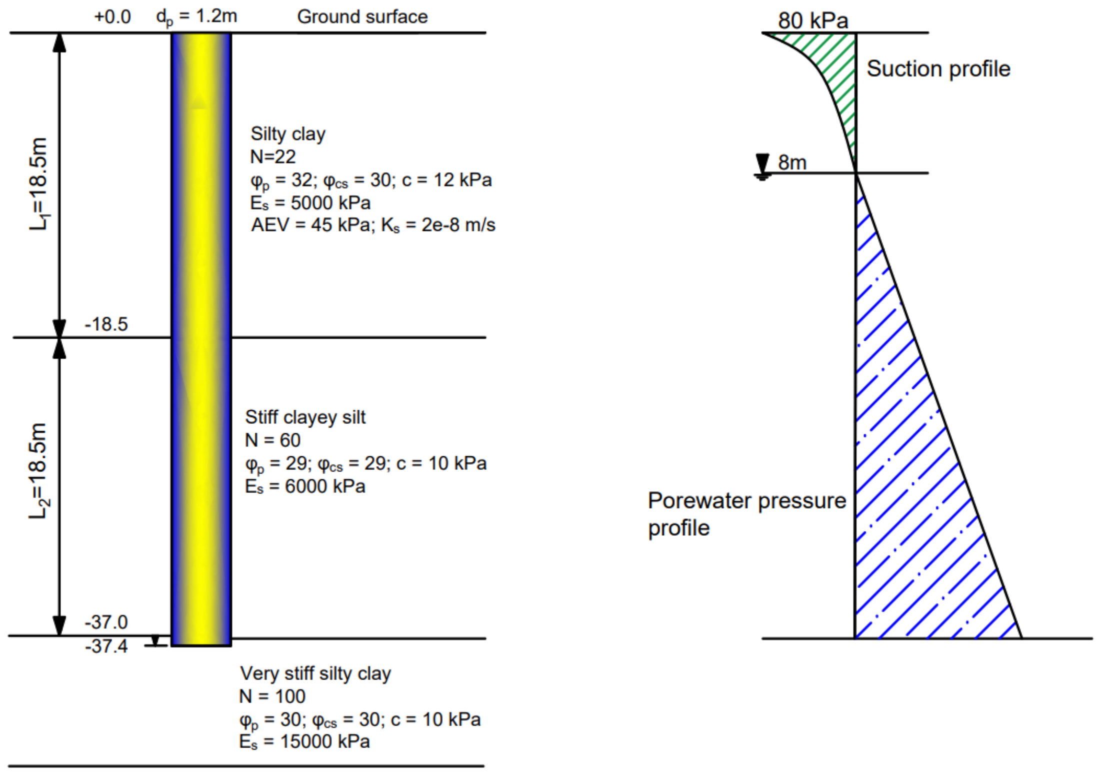

+0.0
d_p = 1.2m
Ground surface
L_1=18.5m
Silty clay
N=22
φ_p = 32; φ_{cs} = 30; c = 12 kPa
E_s = 5000 kPa
AEV = 45 kPa; K_s = 2e-8 m/s
-18.5
L_2=18.5m
Stiff clayey silt
N = 60
φ_p = 29; φ_{cs} = 29; c = 10 kPa
E_s = 6000 kPa
-37.0
-37.4
Very stiff silty clay
N = 100
φ_p = 30; φ_{cs} = 30; c = 10 kPa
E_s = 15000 kPa
80 kPa
Suction profile
8m
Porewater pressure profile

a)

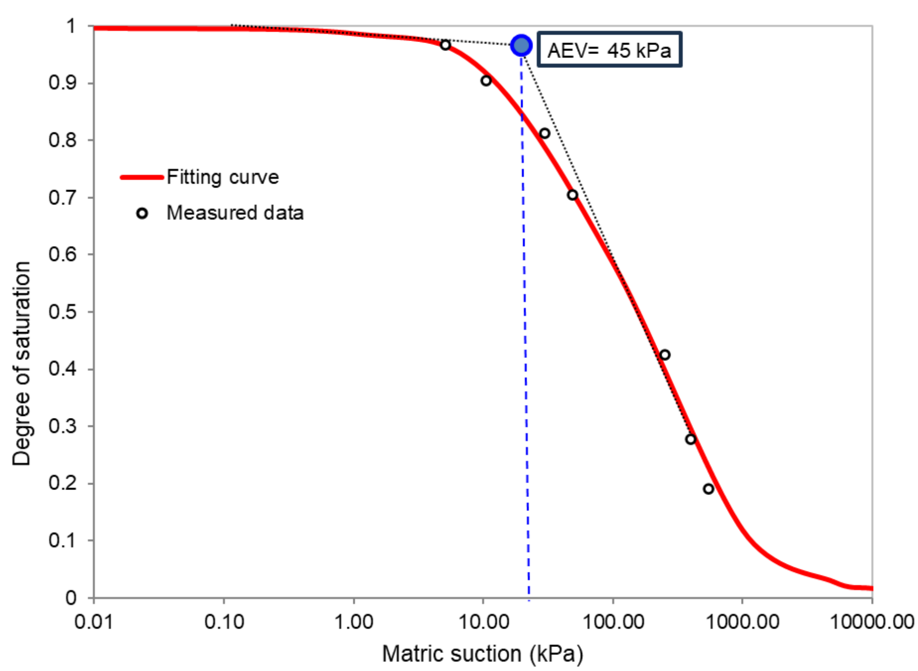

AEV= 45 kPa
Fitting curve
Measured data
Degree of saturation
1
0.9
0.8
0.7
0.6
0.5
0.4
0.3
0.2
0.1
0
0.01
0.10
1.00
10.00
100.00
1000.00
10000.00
Matric suction (kPa)

b)

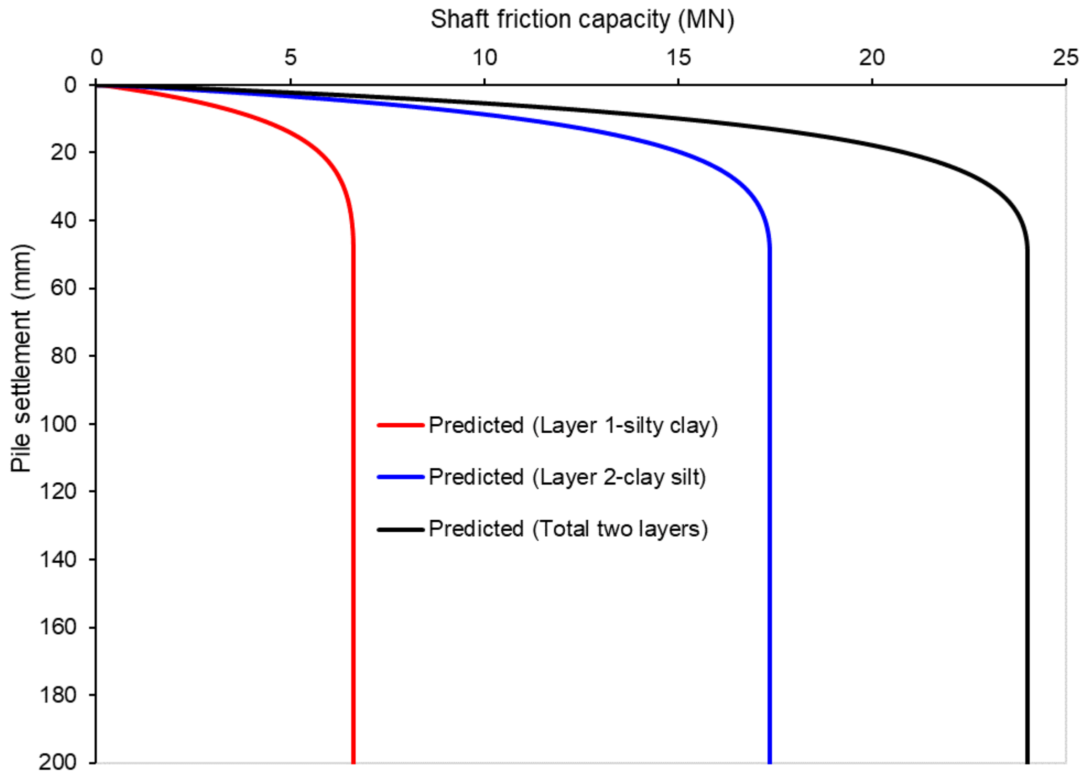
Shaft friction capacity (MN)
0
5
10
15
20
25
0
20
40
60
80
100
120
140
160
180
200
Pile settlement (mm)
Predicted (Layer 1-silty clay)
Predicted (Layer 2-clay silt)
Predicted (Total two layers)

c)

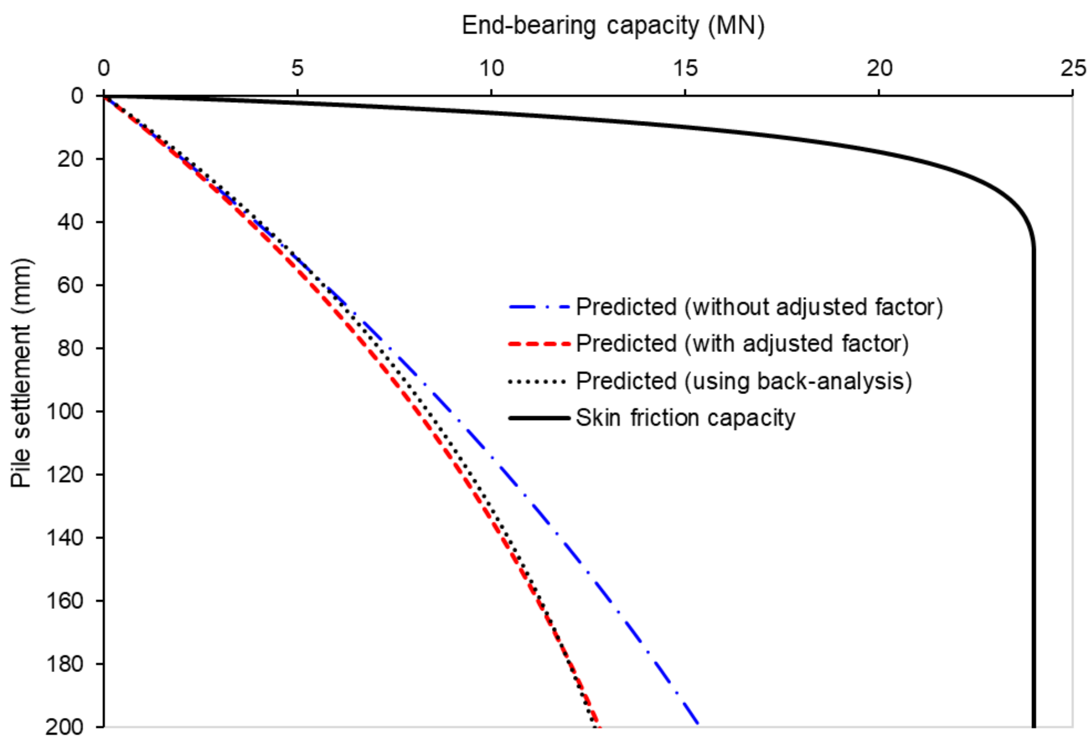
End-bearing capacity (MN)
0
5
10
15
20
25
0
20
40
60
80
100
120
140
160
180
200
Pile settlement (mm)
Predicted (without adjusted factor)
Predicted (with adjusted factor)
Predicted (using back-analysis)
Skin friction capacity

d)

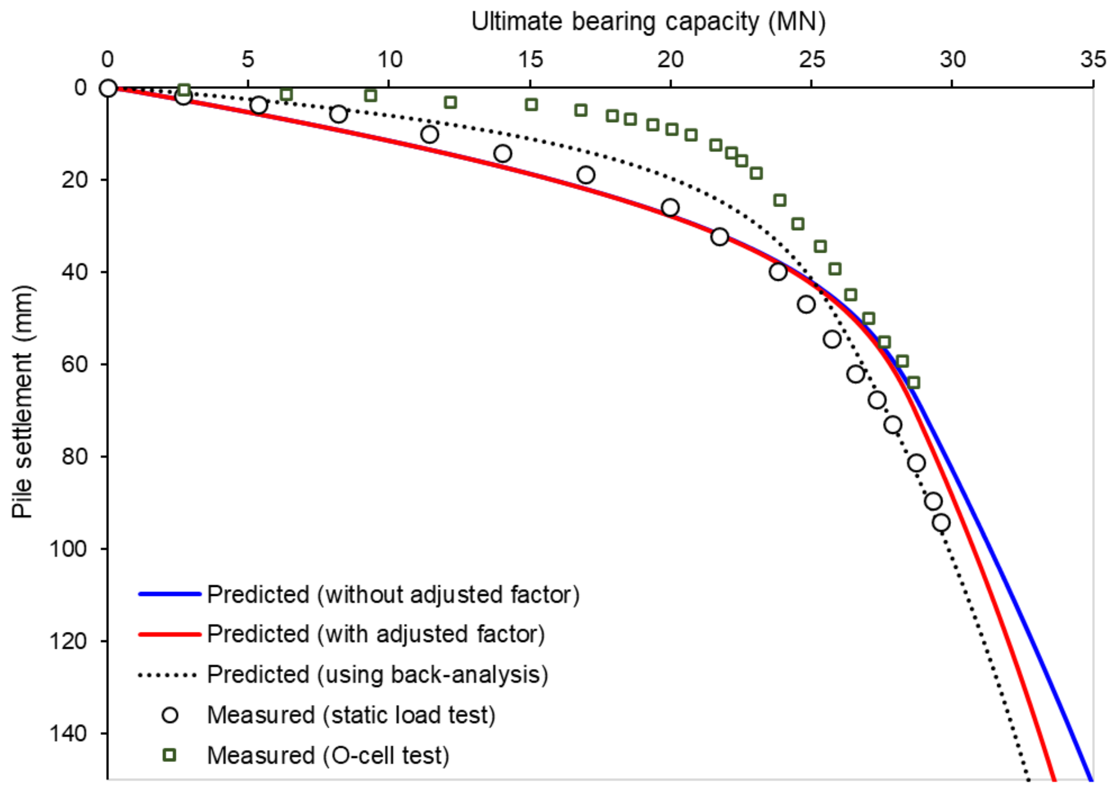

e)

Figure 23. Comparison of predicted and measured results for test pile in Singapore (data after Lee and Park 2008): a) pile test profile, b) SWCC data; c) skin friction capacity, d) End-bearing capacity, e) ultimate bearing capacity

5. Conclusions

To represent the hardening-softening behaviour, an interface shear stress-displacement model was developed using the adhesion-friction integration and disturbed state concept. The only additional parameter in the proposed model was the "ultimate disturbance function" which can be easily determined using either conventional direct shear tests or soil shear strength parameters. The new model captured the hardening-softening behaviour, which is not possible through the use of hyperbolic models.

The experimental results from direct shear tests were used to validate the DSC interface model. The comparison results demonstrated that the shear stress-displacement curve can be successfully simulated and that the proposed model had a better performance compared to the hyperbolic model for both loose and dense soils.

The proposed interface model was extended to integrate with bearing capacity theory to develop the load transfer framework for pile foundations. In this study, a simplified approach was presented, which takes into account the hardening relationship of the base reaction and the nonlinear softening relationship of skin friction. This work also developed prediction methods for the profile of steady-state matric suction in situ, soil-water characteristic curve, and pore-water pressure of unsaturated soils The present method was validated with five well-documented field measurement projects. The comparison results showed that the proposed approach and the behaviour observed in the field were in good agreement.

The proposed analytical approach and developed algorithm provided a cost-effective and reliable solution that was appropriate for the analysis of piles embedded in saturated and unsaturated multi-layered soils.

.

Conflict of Interest

The authors declare that there have no known competing financial interests or personal relationships that could have appeared to influence the work reported in this paper.

Data Availability Statement

All data, models, and code generated or used during the study appear in the submitted article.

Appendix A. Static load test dataset

Table A1. Static load test dataset for analysis of bearing capacity factor N_q

Appendix B. Empirical correlation

Table B1. Empirical correlation between N_{SPT} and shear strength parameters

List of Figures Caption

Figure 11. Schematic of mobilized load-settlement curves for a single pile: (a) skin friction versus displacement; (b) base resistance versus displacement; (c) total bearing capacity versus displacement

Figure 12. Soil phases in idealized soil model: a) saturated soil and b) unsaturated soil

Figure 13. Illustration of SWCC for unsaturated soils

Figure 14. Suction distribution profile with different boundary conditions

Figure 15. An example of suction profile estimation using analytical equation (Eq. 45)

Figure 16. The correlation between the adjusted coefficient and vertical effective stress

Figure 17. Schematic of typical force equilibrium analysis of pile

Figure 18. Flow chart for load-settlement response analysis of piles

Figure 19. Comparison of predicted and measured results for test pile in Shanghai (test data after Feng et al. 2024): a) pile test profile, b) interface shear test results, c) load-settlement curve

Figure 20. Comparison of predicted and measured results for test pile in Italy (test data after Caputo et al. 1991): a) pile test profile, b) skin friction capacity, c) end-bearing capacity, d) ultimate bearing capacity for pile with a diameter of 1.5m, e) ultimate bearing capacity for pile with a diameter of 2m

Figure 21. Comparison of predicted and measured results for test pile in Indiana (test data after Lee et al. 2003): a) pile test profile, b) skin friction capacity, c) end-bearing capacity, d) ultimate bearing capacity

Figure 22. Comparison of predicted and measured results for test pile in Idaho (test data after Fellenius et al. 2004): a) pile test profile, b) skin friction capacity, c) End-bearing capacity, d) ultimate bearing capacity

Figure 23. Comparison of predicted and measured results for test pile in Singapore (test data after Lee and Park 2008): a) pile test profile, b) SWCC data, c) skin friction capacity, d) End-bearing capacity, e) ultimate bearing capacity

References

Alawneh, A. S., Nusier, O., Husein Malkawi, A. I., & Al-Kateeb, M. (2001). Axial compressive capacity of driven piles in sand: a method including post-driving residual stresses. *Canadian Geotechnical Journal*, *38*(2), 364-377.

Al-Shafei, K. A., Cox, W. R., & Helfrich, S. C. (1994, May). Pile load tests in dense sand: Analysis of static test results. In *Offshore Technology Conference* (pp. OTC-7381). OTC.

Ali, H., Reiffsteck, P., Baguelin, F., van de Graaf, H., Bacconnet, C., & Gourves, R. (2010, May). Settlement of pile using cone loading test: Load settlement curve approach. In *CPT'10: 2nd Int. Symp. on Cone Penetration Testing*.

Azzouz, A. S., Baligh, M. M., & Ladd, C. C. (1981). Cone penetration and engineering properties of the soft Orinoco clay.

Baldi, G., Bellotti, R., Ghionna, N., & Jamiolkowski, M. (1989). Stiffness of sands from CPT, SPT and DMT—A critical review. In *Penetration testing in the UK: Proceedings of the geotechnology conference organized by the Institution of Civil Engineers and held in Birmingham on 6–8 July 1988* (pp. 299-305). Thomas Telford Publishing.

Baghini, E. G., Toufigh, M. M., & Toufigh, V. (2018). Analysis of pile foundations using natural element method with disturbed state concept. *Computers and Geotechnics*, *96*, 178-188. https://doi.org/10.1016/j.compgeo.2017.11.005

Budhu, M. (2010). *Soil mechanics and foundations*. John Wiley and Sons.

Bui, T. Y., Li, Y., Tan, S. A., & Leung, C. F. (2005). Back analysis of O-cell pile load test using FEM. In *Proceedings of the 16th International Conference on Soil Mechanics and Geotechnical Engineering* (pp. 1959-1962). IOS Press.

Bohn, C., Lopes dos Santos, A., & Frank, R. (2017). Development of axial pile load transfer curves based on instrumented load tests. *Journal of Geotechnical and Geoenvironmental Engineering*, *143*(1), 04016081.

Brown, M. J., Hyde, A. F. L., & Anderson, W. F. (2006). Analysis of a rapid load test on an instrumented bored pile in clay. *Geotechnique*, *56*(9), 627-638.

Briaud, J. L., Ballouz, M., & Nasr, G. (2000). Static capacity prediction by dynamic methods for three bored piles. *Journal of Geotechnical and Geoenvironmental engineering*, *126*(7), 640-649. https://doi.org/10.1061/(ASCE)1090-0241(2000)126:7(640)

British Standards Institution (2010). *Code of Practice for Strengthened/reinforced Soils and Other Fills: BS 8006-1: 2010*. BSI. London, UK.

Brooks, R. H., and Corey, A. T. (1964). "Hydraulic properties of porous media."*Hydro. Paper No. 3*, Colorado State Univ., Fort Collins, Colorado, USA.

Castelli, F., & Maugeri, M. (2002). Simplified nonlinear analysis for settlement prediction of pile groups. *Journal of geotechnical and geoenvironmental engineering*, *128*(1), 76-84. https://doi.org/10.1061/(ASCE)1090-0241(2002)128:1(76)

Caputo, V. (1991). Equivalent elastic analysis of settlement for piled foundations. Proc. 10th ECSMFE, Florence, Italy. Vol. 4, pp. 1346-1348.

Chen, C., Zhu, S., Zhang, G., Morsy, A. M., Zornberg, J. G., & Mao, F. (2022). A generalized load-transfer modeling framework for tensioned anchors integrating adhesion–friction-based interface model. *International Journal of Geomechanics*, *22*(5), 04022036. https://doi.org/10.1061/(ASCE)GM.1943-5622.0002338

Cho, H. I., Lee, M. G., Sun, C. G., & Kim, H. S. (2021). Evaluation of engineering site conditions in North Gyeongsang Province, South Korea, using a large database of borehole and standard penetration test data. *Engineering Geology*, *294*, 106306.

Chu, L. M., & Yin, J. H. (2005). Comparison of interface shear strength of soil nails measured by both direct shear box tests and pullout tests. *Journal of geotechnical and geoenvironmental engineering*, *131*(9), 1097-1107. https://doi.org/10.1061/(ASCE)1090-0241(2005)131:9(1097)

Coyle, H. M., & Castello, R. R. (1981). New design correlations for piles in sand. *Journal of the Geotechnical Engineering Division*, *107*(7), 965-986.

Cui, Y. L., Qi, C. G., Zheng, J. H., Wang, X. Q., & Zhang, S. M. (2021). Field test research on post-grouting effect for super-long cast-in-place bored pile in thick soft foundation. *Geotechnical and Geological Engineering*, 1-10.

Comodromos, E. M., Anagnostopoulos, C. T., & Georgiadis, M. K. (2003). Numerical assessment of axial pile group response based on load test. *Computers and Geotechnics*, *30*(6), 505-515.

Dai, G., Salgado, R., Gong, W., & Zhang, Y. (2012). Load tests on full-scale bored pile groups. *Canadian geotechnical journal*, *49*(11), 1293-1308.

Dalai, S., & Patra, C. (2021). Prediction of angle of internal friction based on SPT N values. In *Proceedings of the Indian Geotechnical Conference 2019: IGC-2019 Volume V* (pp. 471-477). Springer Singapore.

Desai, C. S. (2001). Mechanics of materials and interfaces: The disturbed state concept. CRC Press, Washington, USA, ISBN 0-8493-0248-X

De Nicola, A., & Randolph, M. F. (1993). Tensile and compressive shaft capacity of piles in sand. *Journal of geotechnical engineering*, *119*(12), 1952-1973. https://doi.org/10.1061/(ASCE)0733-9410(1993)119:12(1952)

Dias, T. G. S., & Bezuijen, A. (2018). Load-transfer method for piles under axial loading and unloading. *Journal of Geotechnical and Geoenvironmental Engineering*, *144*(1), 04017096. https://doi.org/10.1061/(ASCE)GT.1943-5606.0001808

Dithinde, M., Phoon, K. K., De Wet, M., & Retief, J. V. (2011). Characterization of model uncertainty in the static pile design formula. *Journal of Geotechnical and Geoenvironmental Engineering*, *137*(1), 70-85. https://doi.org/10.1061/(ASCE)GT.1943-5606.0000401

Di Donna, A., Ferrari, A., & Laloui, L. (2016). Experimental investigations of the soil–concrete interface: physical mechanisms, cyclic mobilization, and behaviour at different temperatures. *Canadian Geotechnical Journal*, *53*(4), 659-672. https://doi.org/10.1139/cgj-2015-0294@cgj-wgge.issue01

Dunham, J. W. (1954). Pile foundations for buildings. *Proc. ASCE, Soil Mechanics & Foundations Division*, *80*(385).

Edlefsen, N., & Anderson, A. (1943). Thermodynamics of soil moisture. *Hilgardia*, *15*(2), 31-298. https://doi.org/10.3733/hilg.v15n02p031

Eurocode 7: Geotechnical Design. Worked examples. EUR 26227. Luxembourg (Luxembourg): Publications Office of the European Union; 2013. JRC85029

Evgin, E., & Fakharian, K. (1997). Effect of stress paths on the behaviour of sand steel interfaces. *Canadian geotechnical journal*, *33*(6), 853-865. https://doi.org/10.1139/t96-116-336

Farhadi, B., & Lashkari, A. (2017). Influence of soil inherent anisotropy on behavior of crushed sand-steel interfaces. *Soils and Foundations*, *57*(1), 111-125. https://doi.org/10.1016/j.sandf.2017.01.008

Fakharian, K., Meskar, M., & Mohammadlou, A. S. (2014). Effect of surcharge pressure on pile static axial load test results. *International Journal of Geomechanics*, *14*(6), 04014024.

Feng, S., Fang, J., Zhao, Y., Zhang, Z., & Wang, Y. (2024). Thermomechanical Analysis of Energy Piles Using a Load-transfer Approach Considering Soil Coupling Effects. *Computers and Geotechnics*, *168*, 106147. https://doi.org/10.1016/j.compgeo.2024.106147

Feng, S. J., Lu, S. F., & Shi, Z. M. (2016). Field investigations of two super-long steel pipe piles in offshore areas. *Marine Georesources & Geotechnology*, *34*(6), 559-570. https://doi.org/10.1080/1064119X.2015.1038760

Fellenius, B. H., Harris, D. E., & Anderson, D. G. (2004). Static loading test on a 45 m long pipe pile in Sandpoint, Idaho. *Canadian geotechnical journal*, *41*(4), 613-628. https://doi.org/10.1139/t04-012

Fleming, W. G. K. (1992). A new method for single pile settlement prediction and analysis. *Geotechnique*, *42*(3), 411-425. https://doi.org/10.1680/geot.1992.42.3.411

FHWA NHI-06-088, (2006) Federal highway administration US Department. Transp NHI I:2–14. Washington, United state

Fioravante, V. (2002). On the shaft friction modelling of non-displacement piles in sand. *Soils and foundations*, *42*(2), 23-33. https://doi.org/10.3208/sandf.42.2_23

Fredlund, D. G., & Xing, A. (1994). Equations for the soil-water characteristic curve. *Canadian geotechnical journal*, *31*(4), 521-532. https://doi.org/10.1139/t94-061

Gardner, W. R. (1958). Some steady-state solutions of the unsaturated moisture flow equation with application to evaporation from a water table. *Soil science*, *85*(4), 228-232.

Guo, X., Pham, T. A., & Dias, D. (2022). Probabilistic analysis of geosynthetic-reinforced and pile-supported embankments. *Computers and Geotechnics*, *142*, 104595. https://doi.org/10.1016/j.compgeo.2021.104595

Guo, X., Pham, T. A., & Dias, D. (2023). Multi-objective optimization of geosynthetic-reinforced and pile-supported embankments. *Acta Geotechnica*, *18*(7), 3783-3798. https://doi.org/10.1007/s11440-022-01782-4

Hashemi, A., Sutman, M. and Abuel-Naga, H., 2022. Thermomechanical response of kaolin clay-concrete interface in the context of energy geostructures. *Canadian Geotechnical Journal, (ja).*

Hammam, A. H., & Salam, A. A. (2018). Behavior of Bored Piles in Two Soil Layers, Sand Overlaying Compressible Clay (Case Study). In *Advances in Analysis and Design of Deep Foundations: Proceedings of the 1st GeoMEast*

International Congress and Exhibition, Egypt 2017 on Sustainable Civil Infrastructures 1 (pp. 15-27). Springer International Publishing.

Han, F., Prezzi, M., & Salgado, R. (2018). Static and dynamic pile load tests on closed-ended driven pipe pile. In *IFCEE 2018* (pp. 496-506).

Haustorfer, I., & Plesiotis, S. (1988, August). Instrumented dynamic and static pile load testing at two bridge sites. In *Fifth Australia-New Zealand conference on geomechanics: prediction versus performance; preprints of Papers*.

Hara, A., Ohta, T., Niwa, M., Tanaka, S., & Banno, T. (1974). Shear modulus and shear strength of cohesive soils. *Soils and Foundations*, *14*(3), 1-12.

Hatanaka, M., Uchida, A., & Oh-oka, H. (1995). Correlation between the liquefaction strengths of saturated sands obtained by in-situ freezing method and rotary-type triple tube method. *Soils and Foundations*, *35*(2), 67-75..

Heerema, E. P. (1979). Pile driving and static load tests on piles in stiff clay. In *Offshore Technology Conference* (pp. OTC-3490). OTC.

Hirayama, H. (1990). Load-settlement analysis for bored piles using hyperbolic transfer functions. *Soils and Foundations*, *30*(1), 55-64. https://doi.org/10.3208/sandf1972.30.55

Hettiarachchi, H., & Brown, T. (2009). Use of SPT blow counts to estimate shear strength properties of soils: energy balance approach. *Journal of Geotechnical and Geoenvironmental engineering*, *135*(6), 830-834. https://doi.org/10.1061/(ASCE)GT.1943-5606.0000016

Huang, M., Jiang, S., Xu, C., & Xu, D. (2020). A new theoretical settlement model for large step-tapered hollow piles based on disturbed state concept theory. *Computers and Geotechnics*, *124*, 103626. https://doi.org/10.1016/j.compgeo.2020.103626

Hu, L., & Pu, J. (2004). Testing and modeling of soil-structure interface. *Journal of Geotechnical and Geoenvironmental Engineering*, *130*(8), 851-860. https://doi.org/10.1061/(ASCE)1090-0241(2004)130:8(851)

Ismael, N. F. (2001). Axial load tests on bored piles and pile groups in cemented sands. *Journal of geotechnical and geoenvironmental engineering*, *127*(9), 766-773.

Japan Road Association (1990). Specifications for highway bridges. *(Part 4)*, *5*, 38.

Kulhawy, F. H., & Mayne, P. W. (1990). *Manual on estimating soil properties for foundation design* (No. EPRI-EL-6800). Electric Power Research Inst., Palo Alto, CA (USA); Cornell Univ., Ithaca, NY (USA). Geotechnical Engineering Group.

Kumar, R., Bhargava, K., & Choudhury, D. (2016). Estimation of engineering properties of soils from field SPT using random number generation. *INAE Letters*, *1*, 77-84.

Kishida, H., & Uesugi, M. (1987). Tests of the interface between sand and steel in the simple shear apparatus. *Géotechnique*, *37*(1), 45-52. https://doi.org/10.1680/geot.1987.37.1.45

Kim, D., Bica, A. V., Salgado, R., Prezzi, M., & Lee, W. (2009). Load testing of a closed-ended pipe pile driven in multilayered soil. *Journal of geotechnical and geoenvironmental engineering*, *135*(4), 463-473.

Kitiyodom, P., Matsumoto, T., & Kanefusa, N. (2004). Influence of reaction piles on the behaviour of a test pile in static load testing. *Canadian geotechnical journal*, *41*(3), 408-420.

Krasiński, A., & Wiszniewski, M. (2017). Static load test on instrumented pile–field data and numerical simulations. *Studia Geotechnica et Mechanica*, *39*(3), 17-25.

Lee, J., Salgado, R., & Paik, K. (2003). Estimation of load capacity of pipe piles in sand based on cone penetration test results. *Journal of geotechnical and geoenvironmental engineering*, *129*(5), 391-403. https://doi.org/10.1061/(ASCE)1090-0241(2003)129:6(391)

Lehane, B. M., Schneider, J. A., Lim, J. K., & Mortara, G. (2012). Shaft friction from instrumented displacement piles in an uncemented calcareous sand. *Journal of geotechnical and geoenvironmental engineering*, *138*(11), 1357-1368. https://doi.org/10.1061/(ASCE)GT.1943-5606.0000712

Leong, E. C., & Abuel-Naga, H. (2018). Contribution of osmotic suction to shear strength of unsaturated high plasticity silty soil. *Geomechanics for Energy and the Environment*, *15*, 65-73. https://doi.org/10.1016/j.gete.2017.11.002

Lee, J. S., & Park, Y. H. (2008). Equivalent pile load–head settlement curve using a bi-directional pile load test. *Computers and Geotechnics*, *35*(2), 124-133. https://doi.org/10.1016/j.compgeo.2007.06.008

Lee, J., Salgado, R., & Paik, K. (2003). Estimation of load capacity of pipe piles in sand based on cone penetration test results. *Journal of geotechnical and geoenvironmental engineering*, *129*(5), 391-403.

Long, J. H. (2016). *Static pile load tests on driven piles into Intermediate-Geo Materials* (No. WHRP 0092-12-08). University of Illinois at Urbana-Champaign. Dept. of Civil Engineering.

Lu, N., & Griffiths, D. V. (2004). Profiles of steady-state suction stress in unsaturated soils. *Journal of Geotechnical and Geoenvironmental Engineering*, *130*(10), 1063-1076. https://doi.org/10.1061/(ASCE)1090-0241(2004)130:10(1063)

Lu, Y. C., Liu, L. W., Khoshnevisan, S., Ku, C. S., Juang, C. H., & Xiao, S. H. (2023). A new approach to constructing SPT-CPT correlation for sandy soils. *Georisk: Assessment and Management of Risk for Engineered Systems and Geohazards*, *17*(2), 406-422.

Liu, J., Lv, P., Cui, Y., & Liu, J. (2014). Experimental study on direct shear behavior of frozen soil–concrete interface. *Cold regions science and technology*, *104*, 1-6. https://doi.org/10.1016/j.coldregions.2014.04.007

Lv, Y., Liu, H., Ding, X., & Kong, G. (2012). Field tests on bearing characteristics of X-section pile composite foundation. *Journal of Performance of Constructed Facilities*, *26*(2), 180-189.

Martinez, A., & Frost, J. D. (2017). The influence of surface roughness form on the strength of sand–structure interfaces. *Géotechnique Letters*, *7*(1), 104-111. https://doi.org/10.1680/jgele.16.00169

Maghsoodi, S., Cuisinier, O., & Masrouri, F. (2020). Thermal effects on mechanical behaviour of soil–structure interface. *Canadian geotechnical journal*, *57*(1), 32-47. https://doi.org/10.1139/cgj-2018-0583

Mortara, G., Mangiola, A., & Ghionna, V. N. (2007). Cyclic shear stress degradation and post-cyclic behaviour from sand–steel interface direct shear tests. *Canadian Geotechnical Journal*, *44*(7), 739-752. https://doi.org/10.1139/t07-019.

Mandolini, A., & Viggiani, C. (1997). Settlement of piled foundations. *Géotechnique*, *47*(4), 791-816.

Mitchell, J. K., & Soga, K. (2005). *Fundamentals of soil behavior* (Vol. 3, p. USA). New York: John Wiley & Sons. ISBN-13: 978-0-471-46302-7

Mullins, G., Winters, D., & Dapp, S. (2006). Predicting end bearing capacity of post-grouted drilled shaft in cohesionless soils. *Journal of Geotechnical and Geoenvironmental Engineering*, *132*(4), 478-487.

Mujtaba, H., Farooq, K., Sivakugan, N., & Das, B. M. (2018). Evaluation of relative density and friction angle based on SPT-N values. *KSCE Journal of Civil Engineering*, *22*, 572-581.

Nanda, S., & Patra, N. R. (2014). Theoretical load-transfer curves along piles considering soil nonlinearity. *Journal of Geotechnical and Geoenvironmental Engineering*, *140*(1), 91-101.

Nguyen, H. M., Fellenius, B. H., Puppala, A. J., Nguyen, O. C., & Bheemasetti, T. V. (2018). Results of static loading tests on single piles and on pile-supported LPG tanks. *Geotechnical and Geological Engineering*, *36*, 3811-3822.

O'Neill, M. W. (2001). Side resistance in piles and drilled shafts. *Journal of Geotechnical and Geoenvironmental Engineering*, *127*(1), 3-16. https://doi.org/10.1061/(ASCE)1090-0241(2001)127:1(3)

Uchaipichat, A., & Khalili, N. (2009). Experimental investigation of thermo-hydro-mechanical behaviour of an unsaturated silt. *Géotechnique*, *59*(4), 339-353. https://doi.org/10.1680/geot.2009.59.4.339

Uesugi, M., Kishida, H., & Uchikawa, Y. (1990). Friction between dry sand and concrete under monotonic and repeated loading. *Soils and Foundations*, *30*(1), 115-128. https://doi.org/10.3208/sandf1972.30.115

Park, D., & Lee, J. (2015). Comparative analysis of various interaction effects for piled rafts in sands using centrifuge tests. *Journal of Geotechnical and Geoenvironmental Engineering*, *141*(1), 04014082.

Paik, K., & Salgado, R. (2003). Determination of bearing capacity of open-ended piles in sand. *Journal of Geotechnical and Geoenvironmental Engineering*, *129*(1), 46-57.

Park, S., Roberts, L. A., & Misra, A. (2012). Design methodology for axially loaded auger cast-in-place and drilled displacement piles. *Journal of geotechnical and geoenvironmental engineering*, *138*(12), 1431-1441.

Park, J. (2017). A comparative study on the bearing capacity of dynamic load test and static load test of PHC bored Pile. *Journal of the Korean geo-environmental society*, *18*(9), 19-31.

Peck, R. B., Hanson, W. E., & Thornburn, T. H. (1991). *Foundation engineering*. John Wiley & Sons.

Poulos, H. G., & Davids, A. J. (2005). Foundation design for the emirates twin towers, Dubai. *Canadian Geotechnical Journal*, *42*(3), 716-730.

Potyondy, J. G. (1961). Skin friction between various soils and construction materials. *Geotechnique*, *11*(4), 339-353. https://doi.org/10.1680/geot.1961.11.4.339

Pham, T. A. (2020a). Analysis of geosynthetic-reinforced pile-supported embankment with soil-structure interaction models. *Computers and Geotechnics*, *121*, 103438. https://doi.org/10.1016/j.compgeo.2020.103438

Pham, T. A. (2020b). Behaviour of piled embankment with multi-interaction arching model. *Géotechnique Letters*, *10*(4), 582-588. https://doi.org/10.1680/jgele.20.00084

Pham, T. A. (2020c). Load-deformation of piled embankments considering geosynthetic membrane effect and interface friction. *Geosynthetics International*, *27*(3), 275-300. https://doi.org/10.1680/jgein.19.00030

Pham, T. A. (2022a). Design and analysis of geosynthetic-reinforced and floating column-supported embankments. *International Journal of Geotechnical Engineering*, *16*(10), 1276-1292. https://doi.org/10.1080/19386362.2021.1997209

Pham, T. A. (2022b). Micromechanical-based shear strength equation considering the stress-state effect for unsaturated soils. *International Journal of Geomechanics*, *22*(9), 06022022. https://doi.org/10.1061/(ASCE)GM.1943-5622.0002495

Pham, T. A., & Dias, D. (2021a). Comparison and evaluation of analytical models for the design of geosynthetic-reinforced and pile-supported embankments. *Geotextiles and Geomembranes*, *49*(3), 528-549. https://doi.org/10.1016/j.geotexmem.2020.11.001

Pham, T. A., & Dias, D. (2021b). 3D numerical study of the performance of geosynthetic-reinforced and pile-supported embankments. *Soils and Foundations*, *61*(5), 1319-1342. https://doi.org/10.1016/j.sandf.2021.07.002

Pham, T. A., & Dias, D. (2022). A simplified model for the analysis of piled embankments considering arching and subsoil consolidation. *Geotextiles and Geomembranes*, *50*(3), 408-431. https://doi.org/10.1016/j.geotexmem.2021.12.003

Pham, T. A., Wijesuriya, K., & Dias, D. (2022). Analytical model for the design of piled embankments considering cohesive soils. *Geosynthetics International*, *29*(4), 369-388. https://doi.org/10.1680/jgein.21.00034

Pham, T. A., & Sutman, M. (2022a). An analytical model for predicting the shear strength of unsaturated soils. *Proceedings of the institution of civil engineers-geotechnical engineering*, *176*(4), 369-387. https://doi.org/10.1680/jgeen.21.00135

Pham, T. A., & Sutman, M. (2022b). Disturbed state concept and non-isothermal shear strength model for unsaturated soils. *Bulletin of Engineering Geology and the Environment*, *81*(5), 202. https://doi.org/10.1007/s10064-022-02688-x

Pham, T. A., & Sutman, M. (2023). Modeling the combined effect of initial density and temperature on the soil–water characteristic curve of unsaturated soils. *Acta Geotechnica*, *18*(12), 6427-6455. https://doi.org/10.1007/s11440-023-01920-6

Pham, T. A., Hashemi, A., Sutman, M., & Medero, G. M. (2023a). Effect of temperature on the soil–water retention characteristics in unsaturated soils: Analytical and experimental approaches. *Soils and Foundations*, *63*(3), 101301. https://doi.org/10.1016/j.sandf.2023.101301

Pham, T. A., Sutman, M., & Medero, G. M. (2023b). Validation, reliability, and performance of shear strength models for unsaturated soils. *Geotechnical and Geological Engineering*, *41*(7), 4271-4309. https://doi.org/10.1007/s10706-023-02520-7

Pham, T. A., Sutman, M., & Medero, G. M. (2023c). Density-dependent model of soil–water characteristic curves and application in predicting unsaturated soil–structure bearing resistance. *International Journal of Geomechanics*, *23*(4), 04023017. https://doi.org/10.1061/IJGNAI.GMENG-7504

Pham, T. A., Medero, G. M., & Sutman, M. (2023d). Thermo-hydro-mechanical coupling model of elastic modulus characteristic curve for unsaturated soils. *Computers and Geotechnics*, *162*, 105704. https://doi.org/10.1016/j.compgeo.2023.105704

Pham, T. A., Tran, Q. A., Villard, P., & Dias, D. (2023e). Numerical analysis of geosynthetic-reinforced and pile-supported embankments considering integrated soil-structure interactions. *Geotechnical and Geological Engineering*, 1-22. https://doi.org/10.1007/s10706-023-02564-9

Potyondy, J. G. (1961). Skin friction between various soils and construction materials. *Geotechnique*, *11*(4), 339-353. https://doi.org/10.1680/geot.1961.11.4.339

Puri, N., Prasad, H. D., & Jain, A. (2018). Prediction of geotechnical parameters using machine learning techniques. *Procedia Computer Science*, *125*, 509-517.

Randolph, M. F., & Wroth, C. P. (1978). Analysis of deformation of vertically loaded piles. *Journal of the geotechnical engineering division*, *104*(12), 1465-1488. https://doi.org/10.1061/AJGEB6.0000729

Ravera, E., Sutman, M. and Laloui, L., 2021. Cyclic thermomechanical response of fine-grained soil− concrete interface for energy piles applications. Canadian Geotechnical Journal, 58(8), pp.1216-1230.

Rajagopal, C., Solanki, C. H., & Tandel, Y. K. (2012). Comparison of static and dynamic load test of pile. *Electron. J. Geotech. Eng*, *17*, 1905-1914.

Reese, L. C. (1978). Design and construction of drilled shafts. *Journal of the Geotechnical Engineering Division*, *104*(1), 95-116. https://doi.org/10.1061/AJGEB6.0000579

Reese, L. C., and O'Neill, M. W. (1988). Drilled Shafts: Construction Procedures and Design Methods. Federal Highway Administration, Washington, DC.

Reiffsteck, P., van de Graaf, H., & Jacquard, C. (2018). Bearing Capacity and Settlement of Pile Based on Cone Loading Test. In *Advances in Analysis and Design of Deep Foundations: Proceedings of the 1st GeoMEast International Congress and Exhibition, Egypt 2017 on Sustainable Civil Infrastructures 1* (pp. 44-51). Springer International Publishing.

Robertson, P. K. (2010, May). Soil behaviour type from the CPT: an update. In *2nd International symposium on cone penetration testing* (Vol. 2, No. 56, p. 8). Huntington Beach: Cone Penetration Testing Organizing Committee.

Russo, G. (2013). Experimental investigations and analysis on different pile load testing procedures. *Acta Geotechnica*, *8*, 17-31.

Salari, P., Lashkaripour, G., & Ghafoori, M. (2015). Presentation of empirical equations for estimating internal friction angle of SP and SC soils in Mashhad, Iran using standard penetration and direct shear tests and comparison with previous equations. *International Journal of Geography and Geology*, *4*(5), 89.

Seed, H. B., & Reese, L. C. (1957). The action of soft clay along friction piles. *Transactions of the American Society of Civil Engineers*, *122*(1), 731-754.

Seo, H., Basu, D., Prezzi, M., & Salgado, R. (2009). Load-settlement response of rectangular and circular piles in multilayered soil. *Journal of geotechnical and geoenvironmental engineering*, *135*(3), 420-430. https://doi.org/10.1061/(ASCE)1090-0241(2009)135:3(420)

Seo, H., Prezzi, M., & Salgado, R. (2013). Instrumented static load test on rock-socketed micropile. *Journal of Geotechnical and Geoenvironmental Engineering*, *139*(12), 2037-2047.

Seol, H., Jeong, S., & Cho, S. (2009). Analytical method for load-transfer characteristics of rock-socketed drilled shafts. *Journal of geotechnical and geoenvironmental engineering*, *135*(6), 778-789.

Shioi, Y., & Fukui, J. (2021). Application of N-value to design of foundations in Japan. In *Penetration Testing, volume 1* (pp. 159-164). Routledge.

Sharma, H. D., Harris, M. C., Scott, J. D., & McAllister, K. W. (1986). Bearing capacity of bored cast-in-place concrete piles on oil sand. *Journal of Geotechnical Engineering*, *112*(12), 1101-1116.

Shahri, A. A., Malehmir, A., & Juhlin, C. (2015). Soil classification analysis based on piezocone penetration test data—a case study from a quick-clay landslide site in southwestern Sweden. *Engineering Geology*, *189*, 32-47.

Skempton, A. W. (1986). Standard penetration test procedures and the effects in sands of overburden pressure, relative density, particle size, ageing and overconsolidation. *Geotechnique*, *36*(3), 425-447.

Suzuki, Y., Goto, S., Hatanaka, M., & Tokimatsu, K. (1993). Correlation between strengths and penetration resistances for gravelly soils. *Soils and Foundations*, *33*(1), 92-101.

Tang, C., & Phoon, K. K. (2018). Statistics of model factors and consideration in reliability-based design of axially loaded helical piles. *Journal of geotechnical and geoenvironmental engineering*, *144*(8), 04018050.

Tiwari, B., & Al-Adhadh, A. R. (2014). Influence of relative density on static soil–structure frictional resistance of dry and saturated sand. *Geotechnical and Geological Engineering*, *32*, 411-427. https://doi.org/10.1007/s10706-013-9723-6

Toufigh, V., Masoud Shirkhorshidi, S., & Hosseinali, M. (2017). Experimental investigation and constitutive modeling of polymer concrete and sand interface. *International Journal of Geomechanics*, *17*(1), 04016043. https://doi.org/10.1061/(ASCE)GM.1943-5622.0000695

Van Genuchten, M. T. (1980). A closed-form equation for predicting the hydraulic conductivity of unsaturated soils. *Soil science society of America journal*, *44*(5), 892-898. https://doi.org/10.2136/sssaj1980.03615995004400050002x

Wang, H. L., Zhou, W. H., Yin, Z. Y., & Jie, X. X. (2019). Effect of grain size distribution of sandy soil on shearing behaviors at soil–structure interface. *Journal of Materials in Civil Engineering*, *31*(10), 04019238. https://doi.org/10.1061/(ASCE)MT.1943-5533.0002880

Waite, C.A., Narkiewicz, S.A., and Jones, W.V. 1980. Offshore vertical and lateral pile tests on composite friction piles, Pend Oreille Lake, Idaho. In American Society of Civil Engineers (ASCE), Geotechnical Engineering Division, Convention and Exposition, Portland, Oreg., 14–18 April 1980. ASCE, New York

Wolff, T. F. (1989, June). Pile capacity prediction using parameter functions. In *Predicted and observed axial behavior of piles: results of a pile prediction symposium* (pp. 96-106). ASCE.

Wu, Z., Xu, J., Li, Y., & Wang, S. (2022). Disturbed state concept–based model for the uniaxial strain-softening behavior of fiber-reinforced soil. *International Journal of Geomechanics*, *22*(7), 04022092. https://doi.org/10.1061/(ASCE)GM.1943-5622.0002415.

Xiao, D., Wu, C., & Wu, H. (2018). Experimental study on ultimate capacity of large screw piles in Beijing. In *Advances in Analysis and Design of Deep Foundations: Proceedings of the 1st GeoMEast International Congress and Exhibition, Egypt 2017 on Sustainable Civil Infrastructures 1* (pp. 52-58). Springer International Publishing.

Zhang, Q. Q., Zhang, Z. M., Yu, F., & Liu, J. W. (2010). Field performance of long bored piles within piled rafts. *Proceedings of the Institution of Civil Engineers-Geotechnical Engineering*, *163*(6), 293-305. https://doi.org/10.1680/geng.2010.163.6.293

Zhang, Q. Q., & Zhang, Z. M. (2012). A simplified nonlinear approach for single pile settlement analysis. *Canadian Geotechnical Journal*, *49*(11), 1256-1266. https://doi.org/10.1139/t11-110

Zhang, G. A., & Zhang, J. M. (2006). Monotonic and cyclic tests of interface between structure and gravelly soil. *Soils and Foundations*, *46*(4), 505-518. https://doi.org/10.3208/sandf.46.505

Zhu, S., Chen, C., Mao, F., & Cai, H. (2021). Application of disturbed state concept for load-transfer modeling of recoverable anchors in layer soils. *Computers and Geotechnics*, *137*, 104292. https://doi.org/10.1016/j.compgeo.2021.104292

Zhu, H., & Chang, M. F. (2002). Load transfer curves along bored piles considering modulus degradation. *Journal of Geotechnical and Geoenvironmental Engineering*, *128*(9), 764-77. https://doi.org/10.1061/(ASCE)1090-0241(2002)128:9(764)